High-resolution simulations of a macrotidal estuary using SUNTANS ☆

B. Wang *, O.B. Fringer, S.N. Giddings, D.A. Fong

Environmental Fluid Mechanics Laboratory, Department of Civil and Environmental Engineering, Stanford University, Stanford, CA 94305-4020, USA

ARTICLE INFO

ABSTRACT

The parallel, finite-volume, unstructured-grid SUNTANS model has been employed to study the interaction of the tides with complex bathymetry in the macrotidal Snohomish River estuary. The unstructured grid resolves the large-scale, $O(10 \text{ km})$ tidal dynamics of the estuary while employing 8 m grid-resolution at a specific region of interest in the vicinity of a confluence of two channels and extensive intertidal mudflats to understand detailed local intratidal flow processes. After calibrating tidal forcing parameters to enforce a match between free surface and depth-averaged velocities at several locations throughout the domain, we analyze the complex dynamics of the confluence and show that the exposure of the intertidal mudflats during low tide induces a complex flow reversal. When coupled with the longitudinal salinity gradient, this flow reversal results in a highly variable salinity field, which has profound implications for local mixing, stratification and the occurrence of fine-scale flow structures. This complex flow is then used as a testbed from which to describe several challenges associated with high resolution modeling of macrotidal estuaries, including specification of high resolution bathymetry, specification of the bottom stress, computation of the nonhydrostatic pressure, accurate advection of momentum, and the influence of the freshwater inflow. The results indicate that with high resolution comes the added difficulty of requiring more accurate specification of boundary conditions. In particular, the bottom bathymetry plays the most important role in achieving accurate predictions when high resolution is employed.

© 2008 Elsevier Ltd. All rights reserved.

1. Introduction

While current estuarine models mainly focus on tidal-scale circulation and ocean-estuary exchange processes, flow features on intratidal time scales (within one tidal cycle) associated with local irregular bathymetry are critical to understanding basic hydrodynamics and assessing impacts of engineering activities. This is particularly important in tidal river estuaries with nearby cities whose growing populations often result in substantial alterations to the estuary which can significantly affect the local bathymetry at scales not resolved by larger-scale estuarine models. One such example is the Snohomish River estuary, which is the focus of the present paper. The estuary is the lower mainstem of the Snohomish River, defined by the city of Everett, WA, on the east bank and Jetty Island on the west bank (see Fig. 1). The river discharges into Possession Sound, which is one of the major basins of Puget Sound,

and it is the third largest freshwater source in Puget Sound with an annual mean flow of roughly 300 m³ s⁻¹.

The Snohomish River estuary has a typical river morphology with a curved channel that is roughly 300–400 m wide. The mean depth of the river is less than 5 m while the tidal range is over 4 m during spring tide, resulting in extensive intertidal mudflats and currents that exceed 1.5 m s⁻¹. Because the ratio of the tidal range to the water depth approaches unity, the tide is distorted significantly due to nonlinear processes as it propagates into the estuary. Therefore, the key nonlinear processes, including the advection of momentum, the enhanced celerity of gravity waves due to advection, and frictional effects, play a vital role in determining the tidal currents and scalar and sediment transport (Aubrey and Speer, 1985; Warner et al., 2004). Thus, a fully nonlinear hydrodynamic solver is desired for modeling such a system.

To the north of Jetty Island, there exists a bypass region that connects the Snohomish River to the mouth of Steamboat Slough (a tributary) in Possession Sound (Figs. 1 and 2). The bathymetry at this bifurcation is very complex and can be described by two main features. First, the majority of the bypass region consists of intertidal mudflats, which are submerged during high tide and become dry during low tide. As a result, flow through the bypass ceases due to the exposure of the mudflats during low tide, which leads to highly variable local flow and salinity fields. Second, a rocky sill near the north tip of Jetty Island spans roughly one-third of the Snohomish River channel, and the flow in its vicinity has
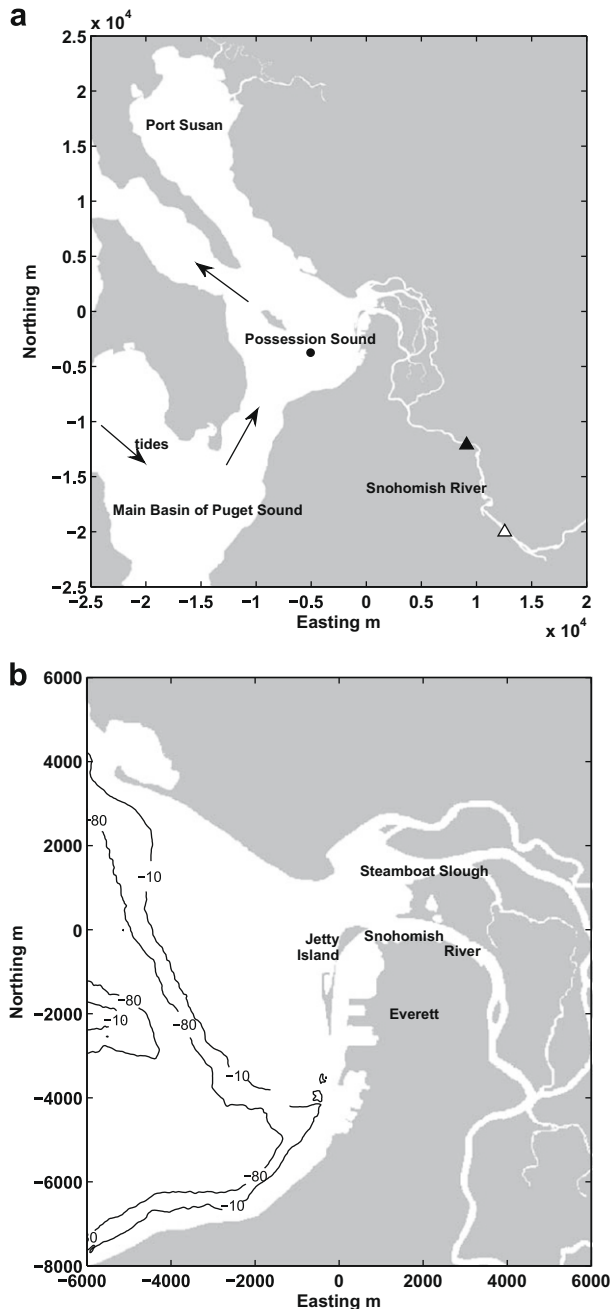
a

b

Fig. 1. (a) Possession Sound and (b) the Snohomish River Estuary. Legend: USGS gage station 12150000 (filled triangle), USGS gage station 12150800 (open triangle), a sample location in Possession Sound used in calibration (filled circle), and the direction of tidal propagation (arrow). Dark zones are highland. Contour-lines on the lower plot are for 10 m and 80 m below Mean Low Low Water (MLLW), respectively. Note that the horizontal axes are northing and easting of UTM Zone 10 N shifted to a location near the north tip of Jetty Island. The origin is located at (558442 m, 5318790 m) in UTM Zone 10 N, and all other figures are plotted relative to this location.

induced considerable scourholes on its northern and southern edges. The spatio-temporal features of the flow at the bypass region and around the abrupt sill have profound implications for the scalar and sediment transport both in the near and far field. In this paper we present the results of applying a highly-resolved, unstructured-grid estuarine model that was developed to (1) accurately represent the tidal dynamics and (2) resolve some of the local dynamics in the bypass junction.

Unstructured grids are well-suited to the present study because of the wide range of spatial scales involved in the system as shown
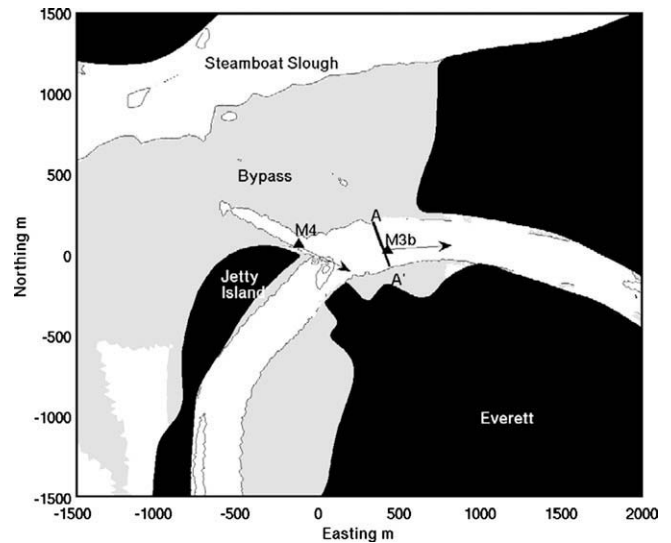

Fig. 2. The bypass region to the north of Jetty Island, showing mooring locations (filled triangles). Arrows define the positive direction of the along-channel velocity. Predictions at transect A-A′ are always taken as viewed in the upstream direction. Black regions are high land, while light grey regions are intertidal zones. Contours are for 12 m, 8 m, 4 m, 0 m below MLLW.

Table 1
Length scales of the features in the Snohomish River estuary

Feature	Approximate length scales
River channel	300 m wide, 5 m deep
Possession Sound	10 km long, 5 km wide, 100 m deep
Salt wedge advection	15 km
Tidal propagation	25–30 km

Values shown are approximate and the exact values vary with the spring-neap cycle and fresh water inflow.

in Table 1. The strong tide propagates more than 30 km upstream as indicated by the observations at USGS gage station 12150000 (location shown in Fig. 1), and the salt intrusion exceeds 12 km as noted by Fram et al., 2003 with field measurements. The primary advantage of unstructured grids is that they can accurately resolve irregular coastlines containing islands and irregular channel junctions while allowing refinement in regions where flow features exhibit high spatial variability (Chen et al., 2003; Pain et al., 2005; Fringer et al., 2006). This allows computational resources to be focused only where they are necessary, thereby greatly increasing computational efficiency.

There has been a tremendous effort in developing field-scale numerical models to understand the estuarine hydrodynamics with an emphasis on the estuary-scale tidal dynamics. To name a few examples, Brooks et al., 1999 studied the tidal flushing and exchange processes in Cobscook Bay using the Princeton Ocean Model (POM) (Blumberg and Mellor, 1987); Gross et al., 1999 implemented the tidal, residual, and intertidal mudflat model (TRIM3D) (Casulli and Cattani, 1994) to study the salinity dynamics in San Francisco Bay over a spring-neap cycle; and Zheng et al., 2003 used the estuarine and coastal circulation model (ECOM-si) (Blumberg, 1993) to investigate the importance of intertidal mudflats on the estuarine circulation, and the water exchange process over the salt marsh of the Satilla River estuary. The work presented here builds on these previous studies and seeks to achieve higher accuracy and resolve processes at smaller scales in time and space. This paper consists of two main parts. In the first part, we describe the setup and validation of the model. In the second part, we discuss challenges associated with high-resolution numerical simulation when high accuracy is sought. In this latter part, the effects of bathymetry, bottom friction, nonhydrostatic pressure, nonlinear

advection of momentum and fresh water inflow are examined via numerical experiments using our model as a test case. While these tests are performed in the Snohomish River estuary, the findings apply to other shallow, mudflat estuaries with strong tides and extensive intertidal mudflats.

2. Hydrodynamic solver

The Stanford Unstructured Nonhydrostatic Terrain-Following Adaptive Navier-Stokes Simulater (SUNTANS) has been implemented to solve the hydrodynamic and transport equations in the present study. It was originally developed by Fringer et al., 2006, and modified by Zhao, 2007 to add the Eulerian–Lagrangian Method (ELM) (Staniforth and Côté, 1991) to solve for advection of momentum in the presence of severe wetting and drying.

SUNTANS is a parallelized model based on a finite-volume framework. It employs a Delaunay-triangulated unstructured grid in the horizontal plane and a structured, z-level grid in the vertical. The structure of the grid follows that described by Perot, 2000 with cell centers defined at the Voronoi points of the triangles. With this setup, orthogonality is satisfied for acute triangles, and more than 99% of the cells we use satisfy this condition. For non-orthogonal cells (obtuse and right triangles), the centers are defined at triangle centroids at the cost of accuracy while ensuring that centers remain within the cells. The advantage of z-levels is that they are simpler to implement with wetting and drying and they do not exhibit the well-known horizontal pressure gradient problem associated with sigma coordinates in the presence of strong bottom slopes (Mellor et al., 1994). However, the disadvantage is a stairlike bottom that leads to a deficiency in resolving the wall-parallel flow in the near-bottom layer.

2.1. Governing equations

The governing equations are the three-dimensional, Reynolds-averaged Navier-Stokes equations under the Boussinesq approximation,

$$\frac{\partial u}{\partial t} + \nabla \cdot (\mathbf{u}u) - fv + bw = -\frac{1}{\rho_0}\frac{\partial p}{\partial x} + \nabla_H \cdot (v_H \nabla_H u) + \frac{\partial}{\partial z}\left(v_V \frac{\partial u}{\partial z}\right), \quad (1)$$

$$\frac{\partial v}{\partial t} + \nabla \cdot (\mathbf{u}v) + fu = -\frac{1}{\rho_0}\frac{\partial p}{\partial y} + \nabla_H \cdot (v_H \nabla_H v) + \frac{\partial}{\partial z}\left(v_V \frac{\partial v}{\partial z}\right), \quad (2)$$

$$\frac{\partial w}{\partial t} + \nabla \cdot (\mathbf{u}w) - bu = -\frac{1}{\rho_0}\frac{\partial p}{\partial z} + \nabla_H \cdot (v_H \nabla_H w),$$
$$+ \frac{\partial}{\partial z}\left(v_V \frac{\partial w}{\partial z}\right) - \frac{g}{\rho_0}(\rho_0 + \rho), \quad (3)$$

subject to incompressibility,

$$\nabla \cdot \mathbf{u} = 0, \quad (4)$$

where $u(x,y,z,t)$, $v(x,y,z,t)$ and $w(x,y,z,t)$ are the Cartesian components of the velocity in the x, y and z directions, i.e., the easting, northing and vertical axes, respectively, and $\mathbf{u}$ is the velocity in vector form. The definitions of the other terms are listed in Table 2. The free surface evolves according to the depth-averaged continuity equation

$$\frac{\partial h}{\partial t} + \frac{\partial}{\partial x}\left(\int_{-d}^{h} u\,dz\right) + \frac{\partial}{\partial y}\left(\int_{-d}^{h} v\,dz\right) = 0, \quad (5)$$

zwhich is obtained by integrating Eq. (4) from the bottom at $z = -d(x,y)$ to the surface at $z = h(x,y,t)$ and then applying the kinematic boundary conditions at $z = h$ and $z = -d$ (see Fringer et al., 2006).

The equation for salinity transport is given by

$$\frac{\partial s}{\partial t} + \nabla \cdot (\mathbf{u}s) = \nabla_H \cdot (\kappa_H \nabla_H s) + \frac{\partial}{\partial z}\left(\gamma_V \frac{\partial s}{\partial z}\right), \quad (6)$$

Table 2
Nomenclature of the terms in the governing equations

u, v, w	Cartesian components of the velocity vector, m s^{-1}
$\mathbf{u}$	velocity vector, m s^{-1}
t	time, s
g	constant of gravitational acceleration, m s^{-2}
ρ_0	the reference density, kg m^{-3}
ρ	density deviation from ρ_0, kg m^{-3}
h	free-surface height relative to some vertical datum, m
d	depth of the bottom relative to some vertical datum, m
p	pressure, pa
s_0	reference salinity, psu
s	salinity, psu
β	saline expansion coefficient, psu^{-1}
f, b	Coriolis coefficients, $f = 2\Omega_{earth}\sin\phi_{lat}$ and $b = 2\Omega_{earth}\cos\phi_{lat}$
Ω_{earth}	the angular velocity of earth rotation, s^{-1}
ϕ_{lat}	the latitude
v_H, v_V	horizontal and vertical eddy viscosities, m^2 s^{-1}
κ_H, κ_V	horizontal and vertical eddy diffusivities for salinity, m^2 s^{-1}

and the density is obtained with a linear equation of state of the form $\rho = \rho_0[1 + \beta(s - s_0)]$. The terms in these equations are defined in Table 2.

2.2. Numerical methods

In SUNTANS, the free surface and vertical diffusion are solved semi-implicitly and thus the propagation of surface gravity waves and vertical diffusion do not constrain the time step size (θ-method, where $\theta = 0.6$ is used) (Casulli, 1990; Fringer et al., 2006). However, in the shallow estuaries, when drying occurs in the intertidal regions, the depth of the water column on the grid becomes small, leading to a highly restrictive Courant condition when explicit Eulerian schemes are used to compute advection of momentum. Zhao, 2007 modified SUNTANS by employing the ELM scheme to compute momentum advection and adapted the code for such drying conditions. The overall accuracy of the method is first-order in time and space and details of the implementation are explained in Zhao, 2007. The ELM scheme is explicit but does not impose a time step limitation if the traceback interpolation schemes are bounded (Casulli, 1990). Due to the low-order interpolation, the ELM scheme forms the leading error in SUNTANS, and the numerical viscosities of ELM can be estimated from those associated with bilinear interpolation on a structured grid, which are $v_{H,num} \sim \frac{\Delta x_i^2}{2\Delta t}C_H(1 - C_H)$ in the horizontal and $v_{V,num} \sim \frac{\Delta z^2}{2\Delta t}C_V(1 - C_V)$ in the vertical (when C_H and C_V are less than unity) (Casulli, 1990), where C_H and C_V are horizontal and vertical Courant number for advection, respectively. In our simulations, for well-resolved areas (10 m resolution), $v_{H,num}$ is estimated to be roughly 1–5 m^2 s^{-1}, and $v_{V,num}$ is of order 10^{-3} m^2 s^{-1} based on mean velocities. Note that using smaller time steps and coarser resolution increases these numerical viscosities. We found that the ELM scheme is slightly more accurate than first-order upwinding when used to compute advection of momentum in lock-exchange problems (not shown).

Assuming the traceback interpolation schemes are bounded and thus do not lead to instabilities, the time step size in SUNTANS is restricted by the explicit horizontal viscosity, horizontal diffusion of scalars, and horizontal advection of scalars (since vertical scalar advection is implicit). The time step is then limited according to

$$\Delta t \leqslant \min\left(\frac{\Delta x_i}{|U_i|}, \frac{\Delta x_i^2}{2\max(v_H, \kappa_H)}\right), \quad (7)$$

where Δx_i is the Voronoi distance between adjacent cells and U_i is the normal velocity on face i.

In estuaries, the propagation of internal waves can be limiting under highly-stratified conditions when the quantity $\epsilon/(vN^2)$ is smaller than 20 (Itsweire et al., 1993). Here ϵ is the dissipation rate,

v is the molecular kinematic viscosity, and N is the buoyancy frequency defined as $N^2 = -(g/\rho)(\frac{\partial \rho}{\partial z})$. In our model, the maximum internal wave speed is roughly $C_i = 0.1$ m s^{-1} during strong stratification assuming a two-layer density profile. Requiring a Courant number less than unity then implies

$$\Delta t \leqslant \min\left(\frac{\Delta x_i}{C_i}\right). \tag{8}$$

Finally, in the presence of wetting and drying, a further constraint is imposed to guarantee that the flux out of one cell during one time step does not exceed the volume of the fluid in that cell. On an unstructured grid, this requires

$$\Delta t \leqslant \min\left(\frac{A_i}{\sum_j L_{ij}|U_{ij}|}\right), \tag{9}$$

where A_i is the planform area of a cell i and L_{ij} is the length of the jth edge and U_{ij} is velocity on the jth edge. The ratio of $A/\sum_j L_j$ is $0.144L$ for equilateral triangles, where L is the edge length, and is smaller (more constraining) for skewed triangles of equal planform area. Although this may appear to be extremely limiting, it assumes the pathological case in which the flux on all cell faces is out of the cell. In practice this condition is rare and it typically suffices to assume the less restrictive case

$$\Delta t \leqslant \min\left(\frac{3A_i}{\sum_j L_{ij}|U_{ij}|}\right), \tag{10}$$

which is equivalent to assuming a restriction of the form $\Delta t < \min(\Delta x_i/|U_i|)$ as in Eq. (7).

2.3. Bottom shear stress

At the bottom boundary, the stress τ_b is computed following the quadratic drag law

$$\tau_b = -\rho_0 C_d |\mathbf{u}|\mathbf{u}. \tag{11}$$

Assuming a velocity profile that satisfies the log law of the form

$$\frac{|\mathbf{u}|}{u_*} = \frac{1}{\kappa} \ln\left(\frac{z}{z_0}\right), \tag{12}$$

where $\mathbf{u}$ is the velocity vector. The drag coefficient C_d is computed from the bottom roughness parameter z_0 in the same way as that in Blumberg and Mellor, 1987 with

$$C_d = \left[\frac{1}{\kappa}\ln\left(\frac{z_b}{z_0}\right)\right]^{-2}, \tag{13}$$

where z_b is the distance of the bottom-most horizontal velocity vector from the bottom, i.e., half of the bottom cell thickness in SUNTANS. The friction velocity is defined by $u_* = \sqrt{|\tau_b|/\rho}$, and κ is the Von Karman constant. Following this formulation for C_d, the computed bottom shear stress is independent of the bottom resolution for a logarithmic velocity profile, which is a necessary condition because the bottom layer thickness varies significantly in the presence of wetting and drying.

We use a roughness parameter of $z_0 = 2.5 \times 10^{-4}$ m inferred from measured velocity profiles at multiple locations in the estuary (Giddings et al., 2008). A larger value ($z_0 = 10^{-3}$ m) is used for the intertidal regions on the fluvial fan offshore from the mouth of Steamboat Slough since it is known to be intensely vegetated with seagrass, which can significantly increase the effective bottom drag (Nepf, 1999). The choice of z_0 is critical for accurate simulation of shallow estuarine flows because friction plays the dominant role in determining energy dissipation and the spatial distribution of tidal amplitude and phase. Zhao, 2007 demonstrated with a numerical model of Elkhorn Slough that doubling the magnitude of z_0 results in noticeable differences in the free surface and tidal cur-

rents, while measurements by Cheng et al., 1993 suggested that the specification of z_0 is not straightforward because it can vary over a tidal cycle by two orders of magnitude. The results of Gross et al., 1999 and Zhao, 2007 both suggest that using a spatially varying z_0 with higher values in shallower regions can significantly improve model results.

2.4. Turbulence closure model

With 30–50 grid cells across the lower part of the main channel and at least 10 cells in the upstream part of the main channel, the most important tidal dispersion processes in the estuary are resolved and the subgrid scale mixing to parameterize is mainly the turbulent diffusion. In our simulations, unresolved horizontal turbulent mixing is represented with a constant eddy-viscosity (v_H in Eqs. (1)–(3)) and eddy-diffusivity (κ_H in Eq. 6). The empirical relationship between the transverse mixing coefficient and the current and water depth in estuaries given by Fischer, 1976 is $\epsilon_t = \beta d u^*$ in the case of shear dispersion, where β is a constant varying from 0.66 to 1.70 for different systems. We estimated ϵ_t is on the order of 0.1 to 1.0 m^2 s^{-1} in our system. Signell and Butman, 1992 also suggested horizontal turbulent mixing coefficients be 0.1–1.0 m^2 s^{-1} for Boston Harbor. Using these estimates as a reference, small explicit horizontal viscosity and diffusivity (0.01 m^2 s^{-1}) are assumed because the numerical viscosity associated with ELM (see Section 2.2) and the first-order upwinding (used for solving advection of scalar transport which is more diffusive than the ELM method (Casulli, 1990)) can provide sufficient mixing.

The vertical viscosity and diffusivity are computed with the Mellor–Yamada level 2.5 (MY2.5) closure scheme (Mellor and Yamada, 1982), with stability functions modified by Galperin et al., 1988. MY2.5 is a two-equation model that computes the evolution of the turbulent kinetic energy ($q^2/2$) and its product with a turbulence macroscale ($q^2 l$). The present implementation follows the formulation in Gross et al., 1999, while we include horizontal advection of q^2 and $q^2 l$. Although MY2.5 has been found to under-predict the eddy viscosity in strongly stratified conditions and over-predict the eddy viscosity in weakly stratified conditions (Stacey et al., 1999), it still gives reasonable salinity and stratification profiles in the present implementation and a variety of others (Gross et al., 1999; Zheng et al., 2003).

2.5. Wet–dry treatment

The intertidal mudflats play a critical role in the present simulations. In general, there are two approaches to simulate wetting and drying, namely (1) the moving-grid method and (2) point-wise treatment on a fixed grid (Ip et al., 1998). The moving-grid approach is more accurate because the grid deforms in order to allow the mesh boundaries to track the free-surface on a boundary-fitted grid (Lynch and Gray, 1980). Although this method is conceptually attractive, it leads to a highly-skewed mesh because the inundation line can be very irregular, and mesh generation is difficult when isolated wet areas form during drying. Furthermore, the computation cost of mesh generation is not trivial in this work due to the complex geometry and resolution requirements, and thus meshing repeatedly can lead to significant overhead.

In this paper we employ a point-wise wet–dry treatment which is a natural choice when z-levels are used. Similar to the work of Ip et al., 1998, we define a buffering layer with thickness h_{buffer} in which the drag coefficient is increased to decelerate the flow when the depth becomes very shallow, thereby alleviating condition (10). In the present formulation we use $h_{\text{buffer}} = 0.05$ m, which is similar to Zheng et al., 2003 (and Ip et al., 1998 used 0.25 m). Zheng et al., 2003 also showed that the result is not sensitive to the choice of h_{buffer}. For cells with water deeper than h_{buffer}, fluxes are

computed with the default drag coefficient from Eq. (13) and the buffering layer has no effect. We further define a minimum depth h_{dry} to ensure positive depth for numerical stability. Cells with depths less than h_{dry} are considered dry and are tagged as inactive until subsequent filling. The choice of h_{dry} is arbitrary and we use 0.002 m which is one order of magnitude greater than the roughness coefficient $z_0 = 2.5 \times 10^{-4}$ m. Fig. 3 illustrates the setup of our wet–dry treatment. This method balances efficiency with accuracy while conserving mass and volume, and it is straightforward to implement within the finite-volume framework of SUNTANS.

3. Setup of the numerical simulation

3.1. Computation domain

With strong tidal forcing and relatively flat bottom topography, tidal signals are strong with roughly 3 m range clearly shown in at USGS gage station 12150000, located 25 km upstream of the river mouth (location shown in Fig. 1(a)). The excursion distance of the salinity front is also significant, and reaches 12 km upstream of the river mouth during high high water (HHW) and 3 km offshore of the river mouth during LLW (Fram et al., 2003). How far the salinity front extends offshore on the fluvial fan is not well known. In order to prevent the salinity front from impinging on the boundaries of the domain, and to avoid complex bathymetry at the boundaries, the computational domain is chosen to include the Snohomish River, Steamboat Slough, Possession Sound and Port Susan (Fig. 1(a)). The computational river channel extends approximately 30 km upstream of the river mouth and ends at USGS gage station 12150800 (location shown in Fig. 1(a)), where tidal oscillations no longer appear in the gage data. The fast decay of the tidal signal from station 12150000 to 12150800 is likely due to the significant increase in the elevation of the river bed.

The complex and inter-connected network of tributaries to the north and east of the bypass region (see Fig. 1) is simplified by merging all of the channels into one single tributary, and this is referred to as Steamboat Slough. This simplification was motivated by a lack of bathymetric data for these regions but is also justified because the details of this region are not crucial for accurately resolving the dynamics of the area of interest. However, accurate representation of tidal-scale and river flow dynamics in Steamboat Slough is necessary to correctly reproduce the tidal dynamics and freshwater flow rates within the Snohomish river, since total freshwater inflow is specified at the upstream open boundary based on the discharge data at gage station 12150800.

Two tidally-forced open boundaries are located at the north and south entrances of Possession Sound, where it connects to Skagit Bay to the north and the main basin of Puget Sound to the south. The sea channels here are relative straight, and the co-phase lines of the tidal waves roughly coincide with the cross-sections (Lavelle et al., 1988), suggesting simplified quasi-one-dimensional along-channel tidal dynamics.
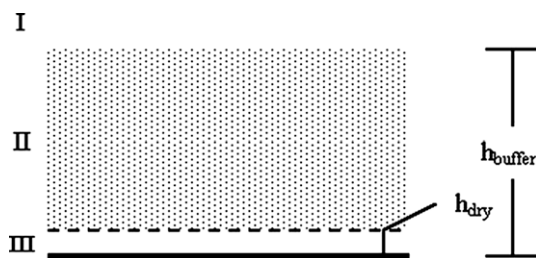

Fig. 3. Schematic of the wet–dry treatment. When the free surface is in zone I, normal bottom drag is used (Eq. 13). In zone II, increased bottom drag is used, and in zone III, the cell is inactive.

Tides in North Puget Sound are formed by long waves propagating into the system from the North Pacific Ocean and through the main basin of Puget Sound from the south (Fig. 1). The majority of North Puget Sound is 100–200 m deep and standing waves are dominant (Mofjeld and Larsen, 1984; Lavelle et al., 1988), with velocity and free surface 90 degrees out of phase. This is evidenced by historical data from Lavelle et al., 1988 which show that the difference in amplitude of the major tidal constituents (M2 and K1) between the two boundaries is less than 0.05 m, and the difference in phase between them is less than 2 degrees. We neglect these minor differences and assume that the domain essentially co-oscillates as a pure standing wave, with the same free surface height, h_{tide}, across the domain. We used the data at Seattle tide station (National Ocean and Atmospheric Administration) which is currently the closest station and accurately represents the tide in Possession Sound. The volumetric tidal fluxes, Q_{tide}, at the boundaries are estimated with

$$Q_{tide} = A_s \frac{dh_{tide}}{dt}, \tag{14}$$

where A_s is the surface area enclosed by the boundary. This surface area decreases as more mudflats are exposed during low tide, but we assume it to be constant for simplicity given that the change in surface area is less than 10% even at extreme low tide (LLW of spring tide). The value of A_s has been calibrated with the free surface in the sound, i.e., h_{tide} is reproduced, and A_s is the only parameter we tuned to calibrate the offshore tidal forcing in the sound.

The direction of the fluxes were determined based on the direction of tidal propagation. During the flood tide, as the tide propagates from south to north in North Puget Sound (see Fig. 1(a)), the flux at the south tidal boundary adds water to the domain while the flux at the north boundary extracts, and the difference between the two fills the domain appropriately. River fluxes are superposed on the tidal fluxes instantaneously to ensure overall volume conservation. According to the residual circulation pattern in Puget Sound described by Cannon, 1983, river fluxes are assumed to drain out to the south. At all three open boundaries, the cross-sectionally averaged velocities are imposed, which are computed by dividing the fluxes by the cross-sectional areas at the boundaries.

3.2. Bathymetry

The model uses a combination of bathymetric data from different sources, which include (1) 30-m resolution bathymetry and topography data by Finlayson, 2005 which covers the entire domain but is not reliable in the shallow regions and river channels; (2) 10-m bathymetry data from a field survey by Giddings et al., 2008, which provides reliable coverage in the lower part of the main channel from the river mouth to approximately 10 km upstream at the bend; (3) 10-m bathymetry data surveyed by Chickadel et al., 2008, which covers the intertidal mudflats around the bypass region. This data is supplemented with some of the very shallow depth inferred based on the waterlines from airborne hyperspectral imagery from Edwards and Jessup, 2008; (4) based on the work of Fram et al., 2003, a constant north–south bottom slope of 10^{-4} is assumed for the remaining part of the river channels not covered by the preceding data sets, and the cross-sections here are treated as rectangular. The overall coverage and resolution of the bathymetry is sufficient for the study in this paper, although we present results which highlight the importance of obtaining detailed bathymetry when employing high-resolution simulations.

3.3. Unstructured grid

We used GAMBIT (Fluent, Inc., Lebanon, NH) to generate the unstructured grid for the present simulations. The finest grid

resolution is 8 m at the bypass junction and this resolution smoothly transitions to 300 m in the Sound, as depicted in Fig. 4. The total number of the horizontal cells is approximately 70,000 with more than 80% located within the estuary and river channels. The vertical resolution is refined in the upper 20 m to resolve the estuarine flow in the vicinity of the bypass region and the layers are stretched beneath that depth. The vertical layer thicknesses are given in Table 3. In total, there are approximately two million three-dimensional grid cells. The depth of the cells are interpolated to the cell centers of the unstructured mesh using the three nearest data points from the bathymetric data described in Section 3.2. The grid employs sufficient resolution to resolve the main bathymetric features of the channel and the mudflats, the main body of the sill and the scourholes at the north tip of Jetty Island.

3.4. Parameterizations and initial conditions

The simulations begin at high high water (HHW) on July 12th, 2006 (year day 192) during spring tide, and end on July 23rd, 2006 (year day 205) which is the following spring tide. Neap tide occurs between year day 196 and 198. A time step of 1 s was used to satisfy the constraints described in Section 2.2, with the drying condition (10) as the most limiting constraint. Using 32 Intel Xeon EM64T (3.6 GHz) processors at the Army Research Laboratory's Major Shared Resource Center (ARL MSRC), nonhydrostatic simulations run as fast as real time, while hydrostatic simulations run roughly 1.8 times as fast as real time.
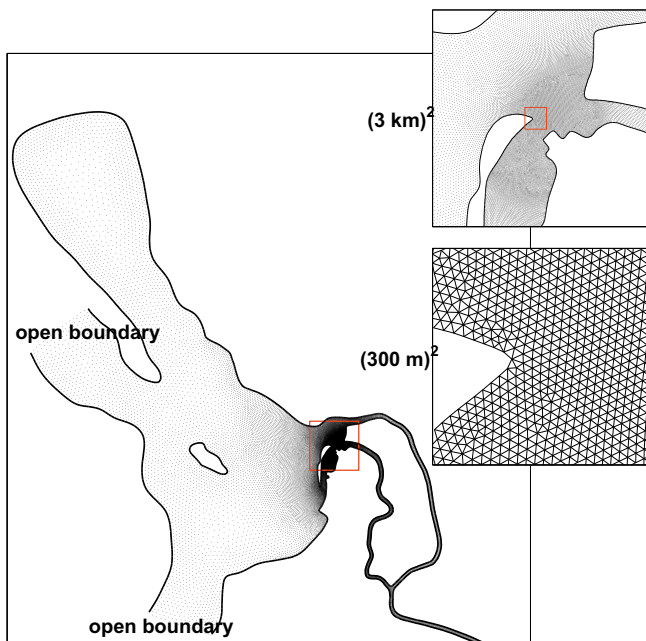

Fig. 4. The unstructured grid of the computational domain. For clarity, only cell centers (Voronoi points) are shown in the left and upper-right panels, while cell edges are shown in the lower-right panel.

Table 3
Vertical resolution of the simulation

Depth (m above MLLW)	Stretch ratio	Thickness (m)
(−1, 4)	1.00	(0.25, 0.25)
(−13, −1)	1.03	(0.25, 0.6)
(−200, −13)	1.19	(0.6, 30)

Top layer of the grid is at 4 m above MLLW. The maximum number of layers is 72.

As discussed in Section 2.4, small values of the horizontal eddy-viscosity and eddy-diffusivity ($\nu_H = \kappa_H = 0.01$ m^2 s^{-1}) were used in the simulations to compromise for the numerical diffusion induced by the ELM scheme in solving the momentum equations and the first-order upwinding scheme in solving the scalar transport equations. Values for the vertical eddy-viscosity and diffusivity were obtained with the Mellor–Yamada 2.5 turbulence closure scheme. Typical values of the eddy-viscosity in the absence of stratification were on the order of 10^{-3} m^2 s^{-1} in the middle of the water column. Temperature and wind effects are not considered in the present simulations because their effects on the large-scale tidal flow are secondary. Specifically, the along-estuary temperature difference is roughly 3 degrees and its effect on density is one order of magnitude smaller than that due to salinity.

The simulation was initialized with a flat free surface and quiescent flow field. The initial salinity field consisted of a uniform horizontal gradient of $\Gamma = 15$ psu km^{-1} at approximately 10 km upstream of the river mouth such that

$$S_0 = \begin{cases} 30, & L < 10 \text{(km)} \\ \Gamma(L-10), & 10 \leqslant L < 12 \text{(km)} \\ 0, & L \geqslant 12 \text{(km)} \end{cases} \qquad (15)$$

where L is the along-river distance from the river mouth in kilometers. The location of this initial gradient is based on the measurements of Fram et al., 2003. The background stratification in Possession Sound is relatively weak with only 3–5 psu difference over 100 m depth (Gustafson et al., 2000). We neglected this minor stratification and assumed a uniform salinity of 30 psu in the sound. Using this initial salinity field, the velocity and salinity fields reach equilibrium in a tidally-averaged sense roughly after one and two tidal cycles, respectively. In the next section, we validate the model by comparing the results from this simulation in hydrostatic mode with field measurements.

4. Model validation

4.1. Free surface

The free-surface predictions were validated with observations (a) in Possession Sound, (b) at gage station 12150000 and (c) at mooring M3b. In Fig. 5(a), the free-surface prediction at a sample location in the sound is compared to the observations in the sound (observations at Seattle tide station were used for the reason explained in Section 3.1). The model successfully captures the co-oscillating behavior of the free surface in the sound which bears a negligible variability in both phase and amplitude throughout the deep offshore regions. Therefore, the choice of the location to validate the predictions in the sound is insignificant, and the sample location we used is indicated by the dark circle in Fig. 1(a). The comparison shows that both the amplitude and phase are accurately predicted, indicating correct specification of the tidal boundary conditions mainly in terms of (1) the assumption of a standing wave and (2) the value of the surface area, A_s (see Section 3.1). In this system, the diurnal (K1) and semi-diurnal (M2) constituents of the tide are comparably strong and as a result strong and weak tides occur within one tidal cycle (see the annotation in Fig. 5(a)) except during the neap tide. Maximum errors of roughly 0.2 m occur during strong ebbs of spring tide. This slight discrepancy is due to the assumption of constant A_s in computing the boundary fluxes, which in reality decreases by roughly 10% due to the exposure of intertidal zones during these low water events especially during the spring tide.

Fig. 5(b) shows the predicted water level at gage station 12150000 (location shown in Fig. 1) in comparison with observations. The prediction has captured the damping and assymetries
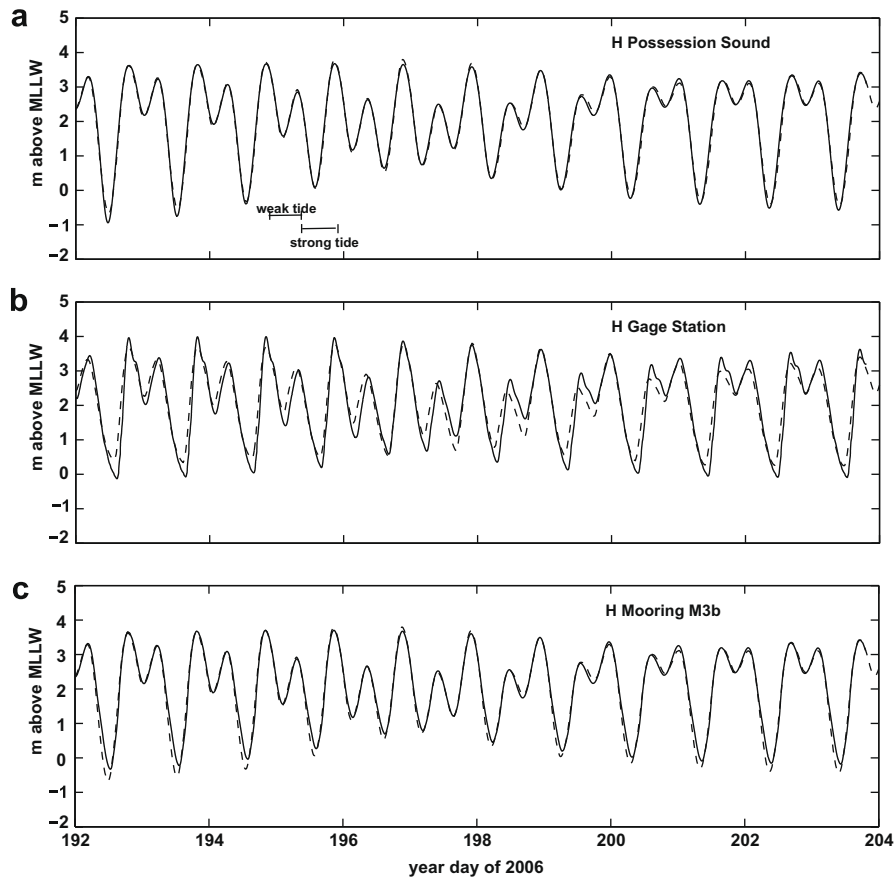
Fig. 5. Comparison of free-surface predictions to observations (a) in Possession Sound, (b) at gage station 12150000, and (c) at mooring M3b. Legend: predictions (–), observations (– –).

of strong ebb tides reasonably well. The errors of phase (roughly lagged by 1 h) and amplitude (roughly over-predicted by 0.5 m) during strong tides are more noticeable than the previous comparison and there is slight distortion of the free-surface variation at high water (HW) after strong floods. These errors are mainly due to the assumption of prismatic geometry (a constant bottom slope and rectangular cross-sections) for a large portion of the upstream river channels and perhaps the simplification of the tributaries, both of which were assumed because of a lack of bathymetric data. These errors can be most severe at the upstream part of the river in a cumulative sense and are considered to have secondary influence on the predictions of the lower estuary. Therefore, despite the errors, we think the propagation of the tides through the river channels is predicted sufficiently well.

Fig. 5(c) shows a comparison of free-surface predictions to measurements at mooring M3b, which is located in the channel near the bypass junction (location shown in Fig. 2). For details of the mooring measurements referred to in this paper, see Giddings et al., 2008. The measurements show that the free surface at M3b is very similar to the offshore tide with a reduction of roughly 0.05 m and a 5 min phase lag for LLW. The comparison shows that there is a slight under-prediction of the amplitude of LLW by roughly 0.3 m (spring tide) and the phase of strong ebbs is lagged by roughly 30 min (spring tide). These errors are likely caused by the numerical dissipation associated with the ELM scheme. It is known that when first-order spatial linear interpolation is used, as in our model, the ELM scheme can induce significant dissipation (McCalpin, 1988; Staniforth and Côté, 1991; Walters et al., 2007), which leads to over-predicted damping of the tidal energy and creates tidal asymmetries. This numerical dissipation can be most sig-

nificant at LLW because strong lateral and vertical shear are induced during this time, which is a result of shallow water depth in the main channels, dry shoals, and ebb currents as strong as 1 m s^{-1}. However, higher-order interpolation methods, e.g., quadratic or high-order kriging methods, are expensive to implement on unstructured grids (Hanert et al., 2005; Wang, 2005), particularly when wetting and drying is employed. Therefore, despite its numerical dissipation, linear interpolation was used in this model.

4.2. Depth-averaged velocities

Comparisons of the predicted and observed depth-averaged along- and cross-channel velocities at moorings M3b (located in the channel) and M4 (in the bypass channel) are illustrated in Figs. 6 and 7, respectively. The location of the moorings are shown in Fig. 2, and both the measured and predicted depth-averaged velocities have been low-pass filtered in time by taking 10-min averages to remove the noise in the field measurements. The along-channel direction is chosen as the principal axis of the tidal ellipsis from the observations (Giddings et al., 2008), and positive velocity is defined as the direction of the flood tide (see Fig. 2). In what follows, it is assumed that the velocity always refers to depth-averages.

At mooring M3b (Fig. 6), both phase and magnitude of velocity are predicted well. The direction of the flow is consistent with the observations, and the most severe errors in the cross-channel velocity, which occur around the time of LLW, are less than 0.1 m s^{-1}. This deviation of the mean flow direction is likely caused by the errors in the predicted flow through the bypass when the bypass becomes very shallow and the mudflats become dry (details of the flow through the bypass will be discussed later in this
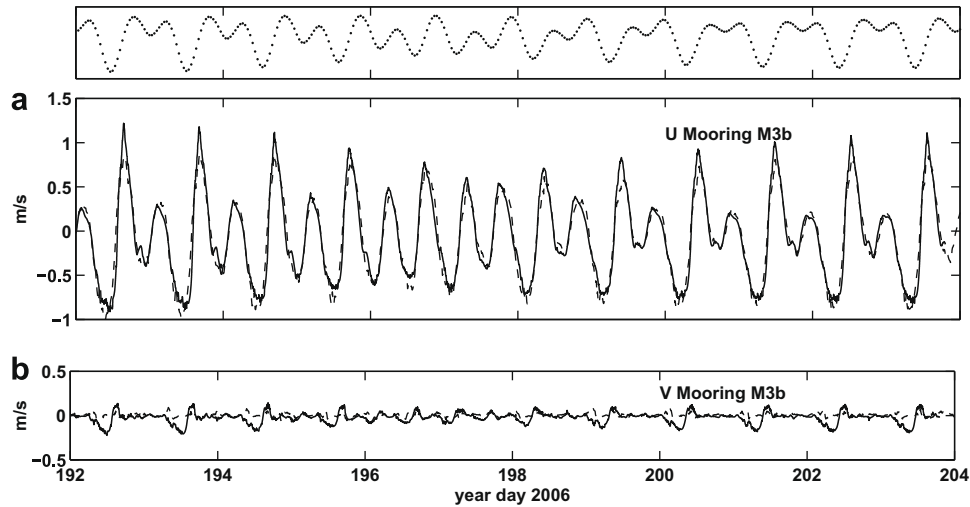
Fig. 6. Depth-averaged (a) along-channel velocity *U* and (b) cross-channel velocity *V* at mooring M3b. Legend: predictions (–), observations (– –), tidal stage (···).

Fig. 7. Depth-averaged (a) along-channel velocity *U* and (b) cross-channel velocity *V* at mooring M4. Legend: predictions (–), observations (– –), tidal stage (···). Arrows in (a) highlight a few of the over-predicted flooding currents in the bypass.
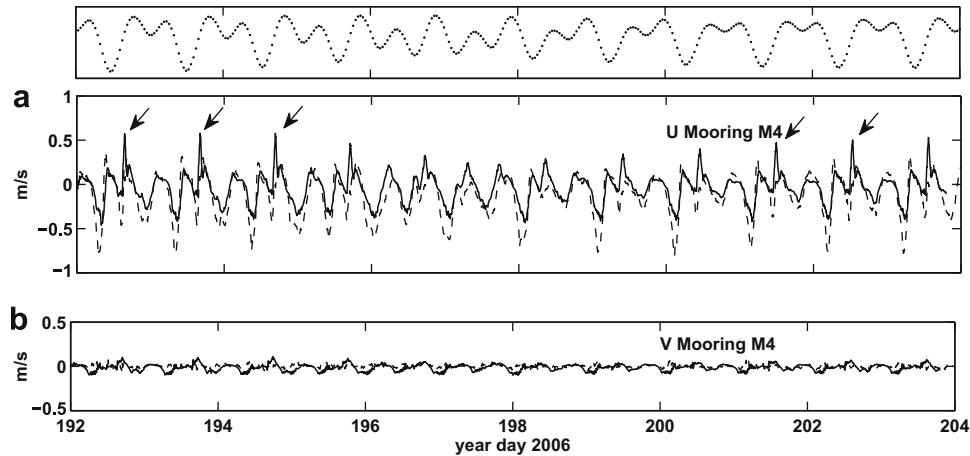
paper). By comparing the velocity and free-surface signals, it is evident that the phase lag between velocity and free surface varies with the tidal stages due to varying degrees of nonlinearity during high tide and low tide: the peak flood currents behave like those in a standing wave, since they occur at an intermediate water level when the free surface is rising fastest, while the peak ebb currents occur at LLW, resembling a progressive wave. The good agreement between model results and observations implies that the model accurately represents the governing nonlinear effects of friction and wave speed.

The comparison shows that some discrepancy exists in the magnitude of peak ebb and flood flows, which may result from various sources. First, the predictions at the mooring location were obtained through an inverse distance-weighted interpolation using the three nearest grid cells. The error of this interpolation, the magnitude of which is a function of the velocity gradients, can be most significant when the currents are strong. Second, the velocities within 0.8 m of the bed are not used in the computation of the depth-average which roughly follows how the measurements were computed (since the ADCPs do not measure this bottom region, as shown in Fig. 8). Thus, the accuracy of the computed depth-averaged velocity is largely dependent upon how well the bottom shear layer is predicted, which is difficult because accurate bottom

boundary layer prediction requires fine resolution near the bed. Finally, numerical errors, such as the dissipation of ELM (see Section 4.1), may contribute to the under-prediction of the ebb tide by extracting tidal energy from the flow. It is worth mentioning that both the measurements and predictions of the velocity show high-frequency oscillations with a period of roughly 30 min during strong ebbs (shown more clearly in Fig. 14(b) around day 195.5). Although we cannot fully explain their origin, we speculate that they are locally-generated resident oscillations in the channel.

The discrepancies in the predicted depth-averaged along-channel velocity at mooring M4 (Fig. 7(a)) are more significant than those at mooring M3b, although the cross-channel velocity shows minimum errors (Fig. 7(b)). The flow at this mooring is highly variable due to the channel bifurcation and a cease and reversal of the bypass flow caused by the exposure of the intertidal mudflats during strong ebbs. During strong ebbs, when the water level drops below roughly 1 m above MLLW, the mudflats surrounding the north end of the bypass region become dry (or too shallow for a considerable amount of flow to pass through) until the free surface rises above that threshold during the flood. During the period of exposure, the flow in the bypass is in the opposite sense relative to its normal ebbing and flooding direction, which is illustrated in Fig. 11 and will be discussed in more detail in Section 5. This
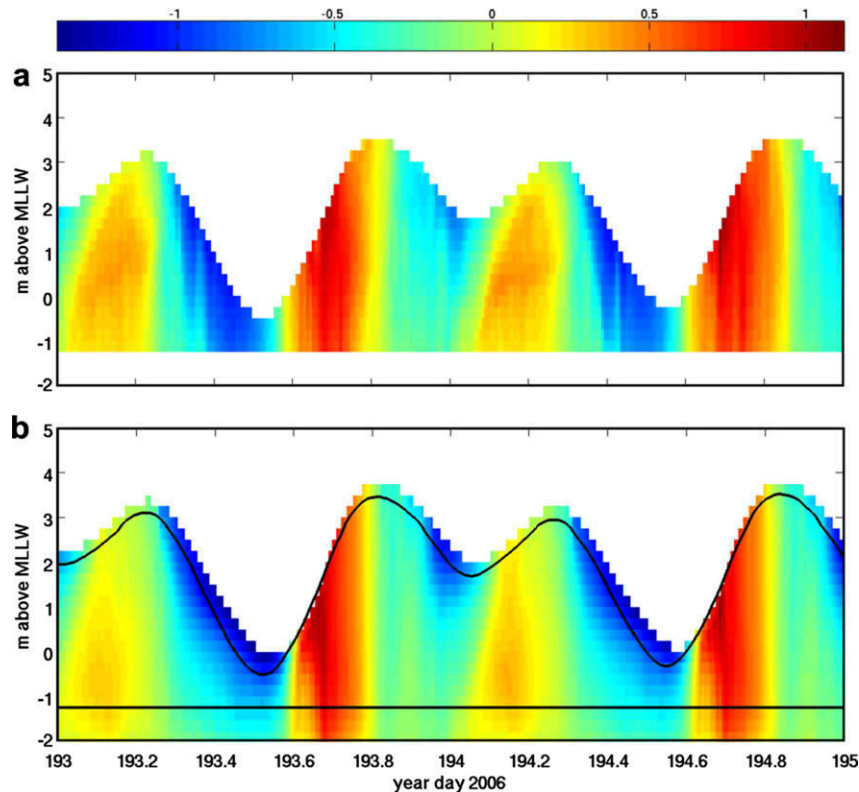
Fig. 8. Time series of the along-channel velocity V(m s^{-1}) at mooring M3b: (a) measurements, (b) model prediction. The range of depth that has been measured (shown in (a)) is between the bold black lines in (b).

complex dynamics in the bypass channel results in a velocity at M4 that varies with a higher frequency than that at M3b. While the present high-frequency behavior is well-predicted by the model from a phasing point of view, the model tends to under-predict the peak ebb velocities and over-predict the flood velocities (Fig. 7). This is exemplified by the spurious peak of positive flow in the prediction during the latter stages of strong floods as indicated by the arrows in Fig. 7(a). Accurately predicting the flow through the bypass channel is much more difficult than the flow in the channel, and four of the major difficulties are highlighted as follows:

(1) The bypass flow is to a large extent controlled by the wetting and drying process on the mudflats. The computation of wetting and drying is subject to larger numerical errors due to the approximations made to ensure numerical stability.

(2) The bypass flow becomes shallower than 1 m during the strong ebb, and the drag coefficients are difficult to parameterize for such shallow flows (Gross, 1997). We suspect that a variable z_0 that depends on the water depth may be necessary to improve the flow prediction as found by Gross, 1997 and Zhao, 2007.

(3) Because the bypass region is small relative to the tidal wave length, a slight difference in the free-surface height across the bypass can drive a relatively strong flow. Thus, the prediction is sensitive to errors on both ends of the bypass, i.e., the main Snohomish River channel to the south and the mouth of Steamboat Slough to the north. We found this to be a good explanation for the suprious peak flood flow at mooring M4, indicated by the arrows in Fig. 7(a). Recall that during strong tides, the model over-predicted the phase lag of the free surface at mooring M3b compared to the offshore tide (see Fig. 5), while the measurements show a much

smaller lag. As a result, in the prediction, during the early stage of the strong flood (before the bypass region becomes submerged), the free surface at M3b is lower (the free surface rises too slow) than the free surface at the mouth of Steamboat Slough by roughly 0.1 m, and thus, at the point when the mudflats become submerged, the free-surface gradient drives a strong north-to-south current through the bypass.

(4) The mouth of Steamboat Slough and the fluvial fan further offshore may be under-resolved in the current simulation because the resolution we chose was primarily to resolve the bypass junction and the tidal flows within the main channel. Therefore, there may be larger errors in the predictions at the north end of the bypass region that influence the predictions in the bypass. However, there are no measurements to verify it at this point.

4.3. Velocity profiles

Time series of the along-channel velocity profile at mooring M3b are depicted in Fig. 8. The predicted velocity structure is generally in good agreement with the measurements. During strong ebbs and floods, when the water column is well-mixed, the single-layer shear flow is well-predicted in the model although the strong flood ends slightly sooner than that in the measurements. During weak tides, however, when stable stratification develops, there are more notable discrepancies in the velocity structure. During the weak ebbs, the magnitude of the ebbing currents in the upper part of the water column, and hence the shear, is over-predicted, while for weak floods, the depth of the point of maximum velocity is greater than that in the measurements. These discrepancies in the predictions of the vertical structure of the velocity are

largely dependent upon how well the turbulence closure scheme can estimate the eddy-viscosity based on shear and stratification. While we discuss the influence of the turbulence model on the stratification and other features of the flow in Section 5, we leave a detailed analysis of the vertical structure of the velocity and eddy-viscosity structures to a future manuscript which focuses on evaluation of several turbulence closure schemes for shallow water estuarine conditions.

4.4. Salinity

Fig. 9 depicts the evolution of the top and bottom salinity at mooring M3b, and Fig. 10 depicts the bottom salinity at mooring M4 (only bottom salinity was measured at mooring M4 due to its shallowness). As shown, the model has captured the general qualitative features of the salinity variations at both moorings and the evolution of the stratification at mooring M3b. At mooring M3b
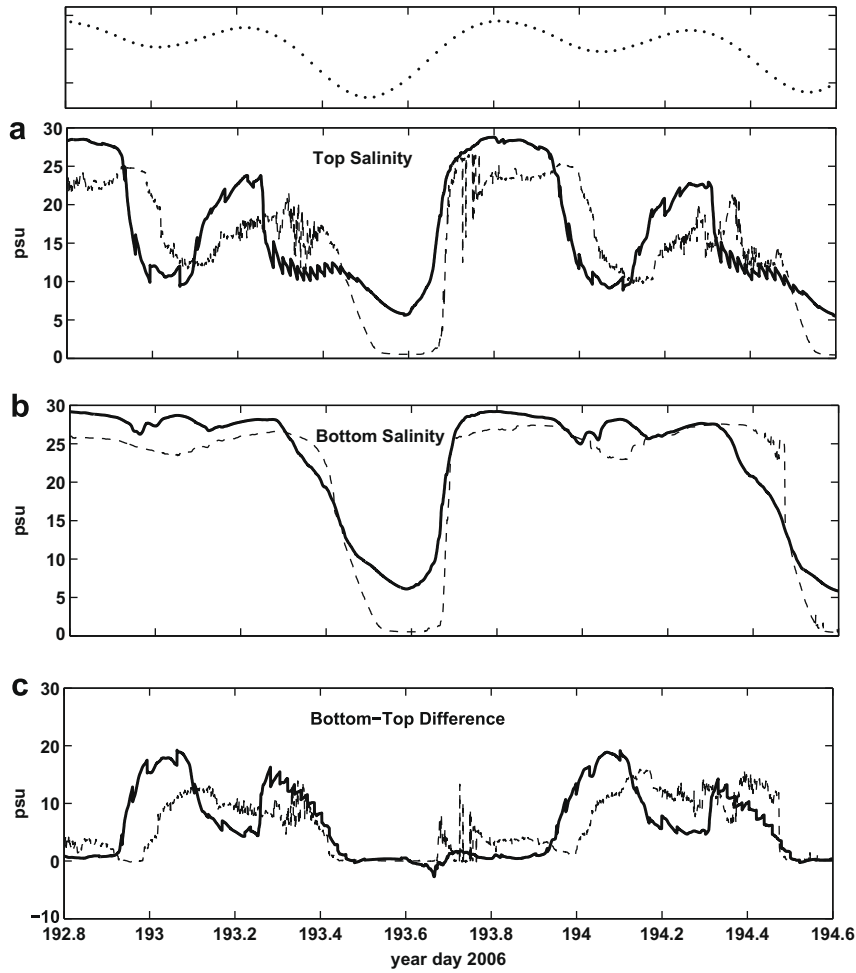

Fig. 9. Time series of salinity at mooring M3b: (a) top salinity, (b) bottom salinity, and (c) top–bottom difference. Legend: prediction (–), observations (– –), tidal stage (⋯).
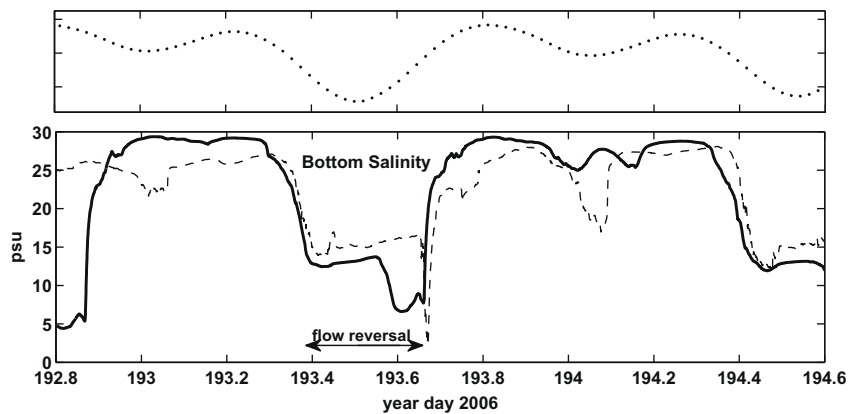

Fig. 10. Time series of bottom salinity at mooring M4. Legend: predictions (–), observations (– –), tidal stage (⋯).

(Fig. 9), the predictions match observations closely during the weak tide, while during the strong tide, the model does not predict zero salinity but a minimum salinity of roughly 5 psu at LLW. This is likely due to insufficient river flow in the main channel (i.e., the fresh water into the slough is over-predicted) and excessive numerical diffusion from the use of first-order upwinding for scalar advection. We chose upwinding in favor of higher-order schemes which are not as efficient, particularly from a conservative point of view, in the presence of wetting and drying. During strong floods, the water column is vertically well-mixed, and a horizontal salinity gradient of approximately 5 psu km^{-1} (measured) is being advected upstream, which was predicted to be 3 psu km^{-1} by the model. In both the prediction and observations, stratification develops during weak ebbs and persists until the late stage of the succeeding strong ebbs when the water column becomes well-mixed. The onset of stratification in the model leads that in the measurements by 1.5 h and the level of stratification in the form of bottom-top salinity difference has been slightly over-predicted. This behavior is consistent with the deficiencies of MY2.5 discovered by Stacey et al., 1999, in that the closure scheme under-estimates the level of mixing during strong stratification, thereby over-predicting the top–bottom salinity difference. At mooring M4 (Fig. 10), the overall pattern of salinity variation is correct and the model has successfully picked up the signals of the flow reversal (see the annotation in Fig. 10). Details of the salinity field in the vicinity of the bypass junction are discussed in Section 5.

These results show that further improvements need to be made for better quantitative salinity predictions. The most critical factors we will consider are the amount of fresh river flow into the main channel and the ability of turbulence closure schemes to predict the mixing level and the onset and breakdown of stratification. It is one of our main future thrusts to evaluate the performance of other two-equation closures, e.g., $k - \omega$, $k - \epsilon$, etc., for such periodically-stratified estuarine conditions. The effects of changing the fresh river inflow are investigated with numerical experiments in Section 6.5.

5. Bypass dynamics

The fine resolution applied at the bypass junction enables the model to capture the complex interaction between the longitudinal salinity gradient and the bypass channel as a combined effect of the tides, the channel bifurcation and wetting and drying of the intertidal mudflats. Fig. 11 illustrates a detailed view of the near-surface salinity at the bypass junction during different stages of a strong ebb tide (around day 193.5) and highlights the complex spatio-temporal variability of the flow and salinity fields due to the flow reversal in the bypass. Fig. 11(a) shows the normal ebb flow directions through the main channel and the bypass. After the bypass channel is shut off during late ebb as a result of the exposure of the mudflats (Fig. 11(b)), the fluid trapped in the bypass region drains back into the main channel. While the flow in the main channel becomes fresher as the ebb continues to advect the salt wedge downstream, the salinity of the bypass flow is relatively constant as the water ponded in the bypass region only varies roughly by 3 psu from the north to the south end of the bypass. Fig. 11(d) shows that after the initiation of the flood, fresher water from the channel fills into the bypass region which causes a sharp decrease in the salinity at mooring M4 as shown by the measurement in Fig. 10 (e.g., the spike of depression around year day 193.7). As the flood tide proceeds, the bypass region becomes deeper and more mudflats become submerged (Fig. 11(e)), such that flood waters increasingly flow through the bypass relative to the main channel. At first, these waters are fresher than those in the channel because they are what had filled into the bypass region earlier(shown in Fig. 11(d)), and they gradually become more sal-

ine as flood waters from farther offshore reach the bypass. At the late stage of flood (Fig. 11(f)), the longitudinal salinity gradient is eventually advected much further upstream and the flows through the bypass and the main channel are both saline.

The convergence of waters of different salinities at the bypass junction appears as a strong transverse salinity gradient in the predictions, as shown by the dashed lines in Fig. 11(e) and (f). This convergence process consistently leads to an axial front that forms during strong floods when the flooding water masses from the bypass region and from the main river channel encounter one-another. During late flood, the front is observable as a surface convergence zone which shows up visually, in radar imagery (Jessup et al., 2006), and in thermal imagery due to the differing temperatures of the water masses (Chickadel et al., 2008; Edwards and Jessup, 2008). As the bypass flow strengthens with the rising water level, the front gradually rotates from its original longitudinal orientation in the east-west direction (Fig. 11(e)) to one that is cross-channel in the northwest–southeast direction (Fig. 11(f)).

In the water column beneath the axial front, a system of two counter-rotating cells has been identified in the field measurements (for details see Giddings et al., 2008) as well as in the model predictions (Fig. 12), and these counter-rotating cells are responsible for the convergence zone on the surface. Such two-cell circulation patterns are commonly observed at Y-shaped channel confluences because of the opposing curvature in the confluent flows (Ashmore, 1982). We speculate that the circulation at the confluence in the present simulations is considerably strengthened by the density-driven circulation (Giddings et al., 2008). The spatio-temporal variability of the flow and salinity fields at the bypass junction have profound implications for the generation of fine-scale turbulence and flow structures in this region. This will be the focus of future simulations on refined grids which we leave for a future manuscript.

It is worth mentioning that while the thermodynamics of the flow around the bypass region is quite complex due to differential heating in the extremely shallow regions and the intertidal mudflats (Edwards and Jessup, 2008), (i.e., shallow waters are more sensitive to diurnal heating and mudflats can retain heat during exposure and release the heat to water when submerged), temperature effects on density are much weaker than those due to salinity. For this reason we have not considered the thermodynamics of the flow at the present stage.

6. Challenges in high-resolution estuarine modeling

When high resolution is employed in estuarine modeling, such as in the present simulations, more care must be taken in model implementation if the end result is to achieve higher spatio-temporal accuracy. In particular, while increased grid resolution reduces the spatial discretization error, which inherently reduces the temporal discretization error for a given Courant number, high resolution imposes greater constraints on the initial and boundary conditions and subgrid-scale parameterizations involved. These constraints present challenges in the implementation of high resolution simulations that are much more significant than when coarser simulations are employed. In this section we discuss five such challenges which have been found to have great impact on the model performance, namely the bathymetry, the bottom drag parameterization, the nonhydrostatic pressure, the advection of momentum, and the freshwater inflow.

6.1. Accurate bathymetry for the intertidal mudflats

Intertidal mudflats are important components in shallow estuaries. In particular, the wetting and drying of the intertidal zones has been found to have significant influence on the tidal currents
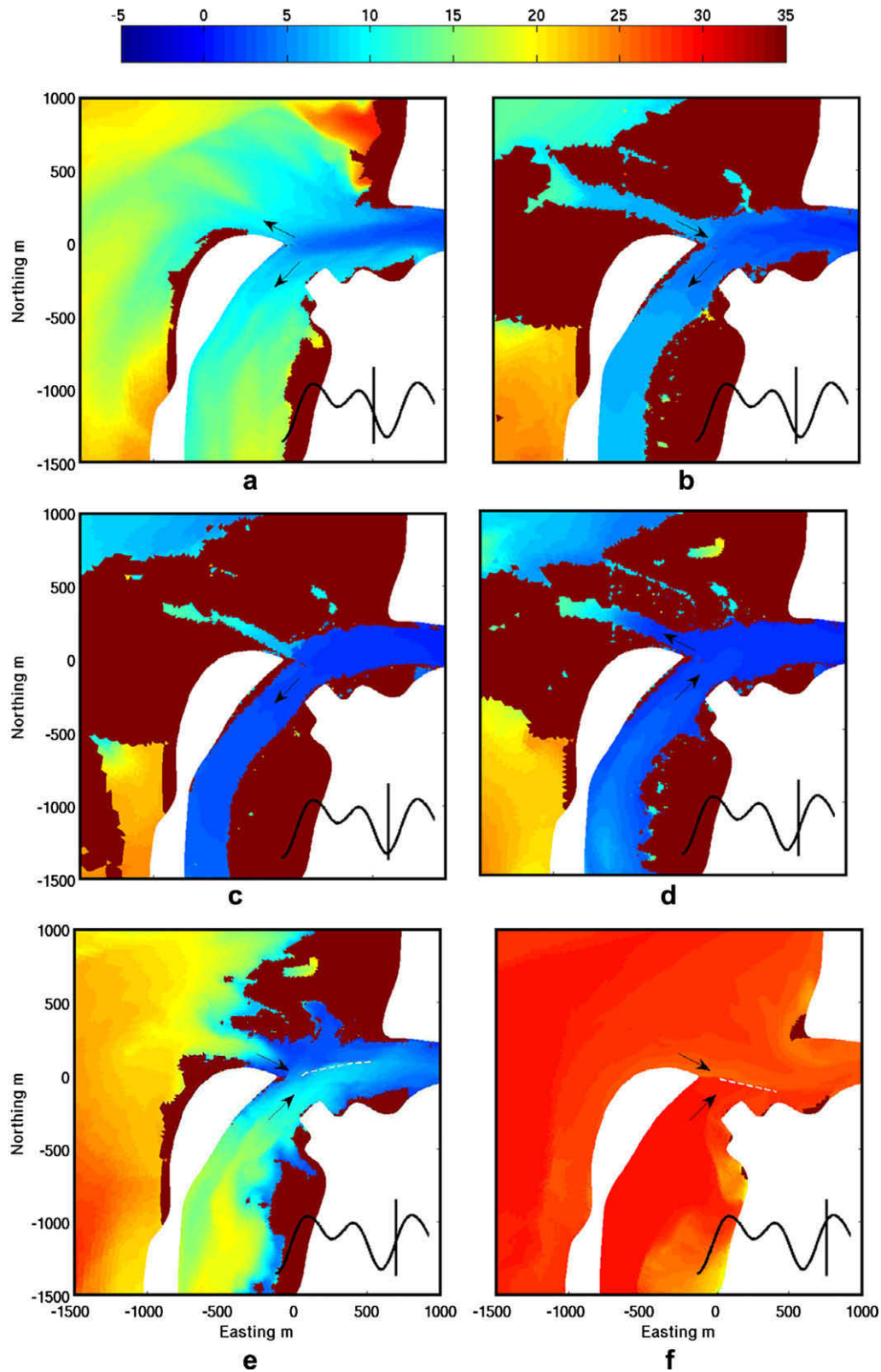
Fig. 11. Near-surface salinity field at the bypass junction at different stages of a strong ebb tide (around day 193.5). Legend: dry areas (dark red), flow direction (arrows), the axial front (white – –) in plots (e) and (f). The color scale from −5 to 35 psu is chosen for the best illustration on the salinity gradient and the predicted range of salinity is shown in Fig. 9. (For interpretation of color mentioned in this figure the reader is referred to the web version of the article.)

(Zheng et al., 2003). During inundation, the mudflats typically remain as the shallowest regions, and dynamics are highly nonlinear and sensitive to slight changes in the depth (Warner et al., 2004). Accurate bathymetric data for the intertidal mudflats is therefore

of major importance in high-resolution numerical simulations. In the present implementation, the flow through the bypass and, indirectly, the flow in the main channel, are strongly dependent upon how well the intertidal mudflats at the mouth of Steamboat Slough
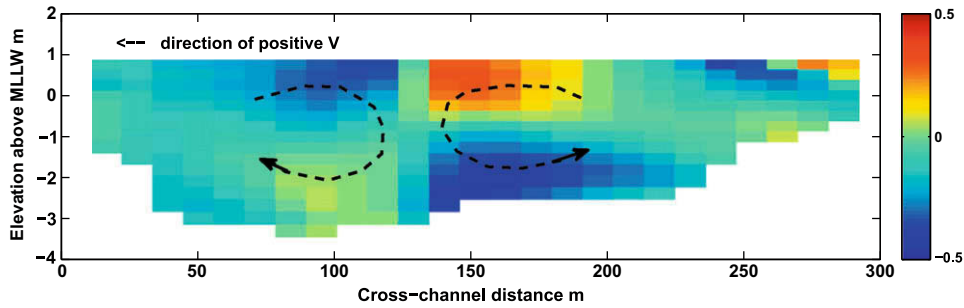
Fig. 12. Cross-channel velocity V(m s^{-1}) showing two counter-rotating circulation cells beneath the axial front at the confluence at transect A-A′ (Fig. 2). Into the page is the upstream direction. The positive direction of the transverse velocity is parallel to transect A-A′ and points towards the outer bank (to the left in the figure).

and on the fluvial fan are represented. The bathymetry that we used before performing more detailed surveys only had accurate survey data up to the north edge of the bypass (indicated by the dashed line in Fig. 13(a); see Section 3.2 for the bathymetric data used in this work), while the shallow areas at the mouth of Steamboat Slough and on the fluvial fan were not well-resolved. The bathymetry in our simulations was improved using new survey data at the mouth of Steamboat Slough, as well as bathymetry estimated from inundation lines using aerial imagery of the fluvial fan. As shown in Fig. 13, the new bathymetry shows remarkable improvement over the old bathymetry. In general, the updated bathymetry is shallower with an average adjustment of +0.3 m in the bottom elevation, and the updated bathymetry resolves more of the intertidal mudflats. Fig. 13 depicts the exposed areas during a strong low tide around day 193.5, and the differences are quite striking. In what follows we compare the results of using the old bathymetry to those with the new bathymetry to highlight the importance of using good bathymetry in high-resolution simulations. Note that, except for this section, the new bathymetry was used in all simulations presented in this paper.

Comparisons of free-surface height and depth-averaged along-channel velocities using the old and new bathymetry are illustrated in Fig. 14. The results show that the flow at mooring M4 is heavily impacted by the bathymetric change as shown in

Fig. 14(c). With the old bathymetry, the peak ebb currents are noticeably stronger and last longer before they eventually reverse direction. This is to be expected, since, with the old bathymetry the areas offshore from the bypass are deeper. The reversed flow with the old bathymetry is also much weaker and this is more apparent as the strong ebb weakens with the progression of spring-neap cycle. Furthermore, by day 195.5, the flow using the old bathymetry no longer reverses at mooring M4 because the north part of the bypass region remains submerged during LLW, so flow through the bypass never shuts off as it should. This effective deepening of the area around mooring M4 due to the unresolved bathymetry effectively causes the flow around mooring M4 to behave much like it does at mooring M3b. Use of unresolved bathymetry also causes an increase in the strength of the flood currents, and in particular the strong peaks during the flood tides.

These results show that the slight deepening of the bathymetry by an average of roughly 0.3 m which results from the use of inaccurate bathymetry has a significant effect on the dynamics of the bypass flow. While the effect of the bathymetry on the flow at mooring M4 is direct, since this mooring sits at the southern edge of the bypass region, the flow at mooring M3b is also influenced, albeit indirectly. The strongest effects occur during late flood after the peak flood (Fig. 14(b)), where the flood current decays sooner and is 0.2 m s^{-1} smaller than that in the simulation with the new
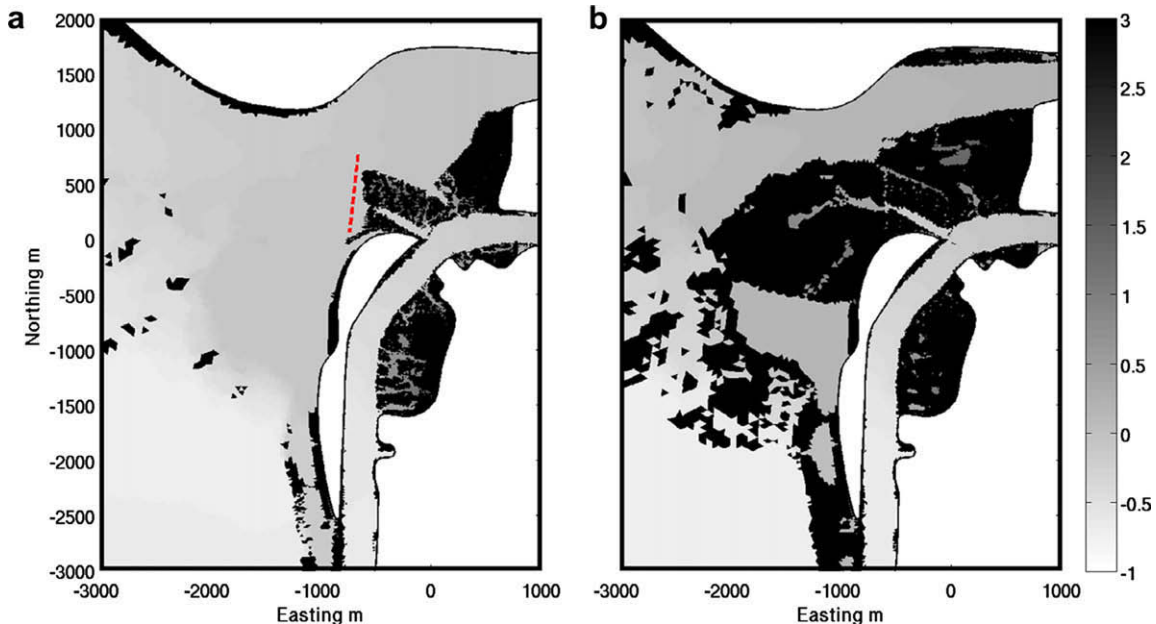

Fig. 13. Intertidal mudflats exposed during LLW on (a) the old bathymetry and (b) the new bathymetry. Free-surface height (m above MLLW) for day 193.5 is plotted on the wet areas. The dashed line in (a) indicates where the old survey data ends.
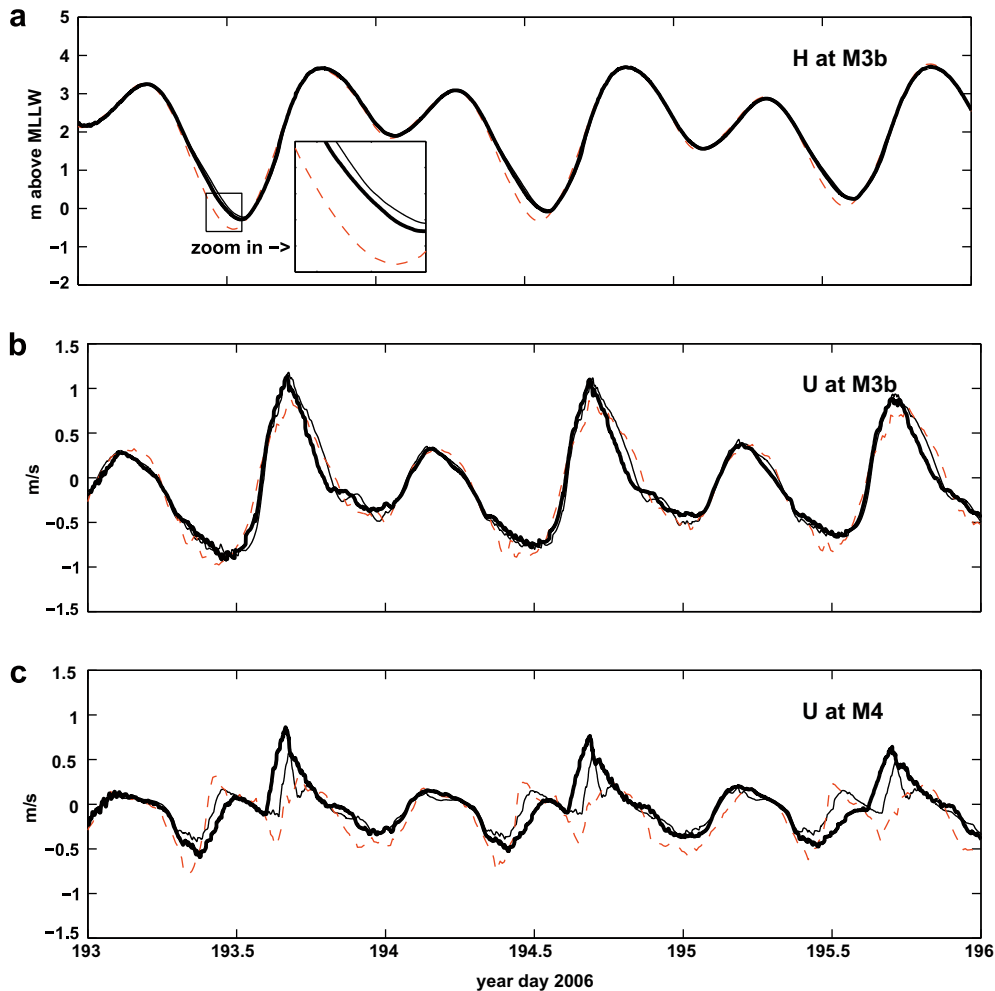
Fig. 14. Time series of (a) free surface at mooring M3b, and depth-averaged along-channel velocity U at (b) mooring M3b and (c) mooring M4. Legend: simulation using the old bathymetry (bold –), simulation using the new bathymetry (thin –), and measurements (thin – –).

bathymetry. Recall that mooring M3b is located closer to the inner bank of the Snohomish River channel (see Fig. 2). The simulations using the old bathymetry show that the stronger flood flow from the bypass quickly raises the free surface in the main channel at the bypass junction, and this impedes the flow in the channel. This is confirmed by enhanced velocities near the outer bank of the Snohomish River and reduced velocities in the downstream reach of the main channel in the model prediction.

While bathymetric changes strongly influence depth-averaged currents, Fig. 14(a) shows that the effect of bathymetric changes on the free surface is small and negligible compared to the tidal range. The largest deviation occurs during strong ebbs (e.g., between time day 193.3 and 193.5), during which time the prediction using the old bathymetry slightly leads that which uses the new bathymetry. This occurs because the ebbing flow through the bypass is stronger and lasts longer when the old bathymetry is used. This discrepancy vanishes when the tide approaches LLW and the bypass flow eventually ceases, and the magnitude of the difference is negligible compared to the lag between the model prediction using the new bathymetry and the measurement at all times (see Section 4.1 for a discussion of this lag).

6.2. Bottom friction

Bottom friction is one of the most important nonlinear mechanisms in the dynamics of shallow flows, and it is thus a critical

parameter in numerical simulations. The effect of bottom friction has an inverse dependence on the water depth and it varies spatially and temporally: it is stronger in shallower regions and it is also stronger during low tide than during high tide (Warner et al., 2004). A test with zero explicit bottom drag, i.e., $C_d = 0$, was performed to demonstrate its effects. The remaining parameterizations and conditions were the same as in the original simulation, and the wet–dry treatment with a frictional buffering layer was still applied as discussed in Section 2.5. The along-channel velocity profile at LLW around day 193.5 at cross-section A-A′ (see Fig. 2) is depicted in Fig. 15. At this time, the ebb current is as strong as $1\ m\ s^{-1}$, and the salinity in the water column is well-mixed so that baroclinic effects are negligible. From the figure one can see that the effect of removing the bottom drag is to reduce the amount of vertical shear throughout the water column, and the vertical shear almost vanishes near the bed. The structure that remains in the flow is likely caused by channel curvature as well as transverse bathymetric variability. The figure also shows that the slow velocity fluid at the edges of the channel persists even after removal of the bottom friction. This slow velocity fluid results from the form drag induced by the stair-stepped grid, which is particularly high at the channel edges where the steep bathymetry is not as well-resolved. Due to the frictional effect of the stair-stepped grid, the effective bottom drag is reduced, but not removed when $C_d = 0$.
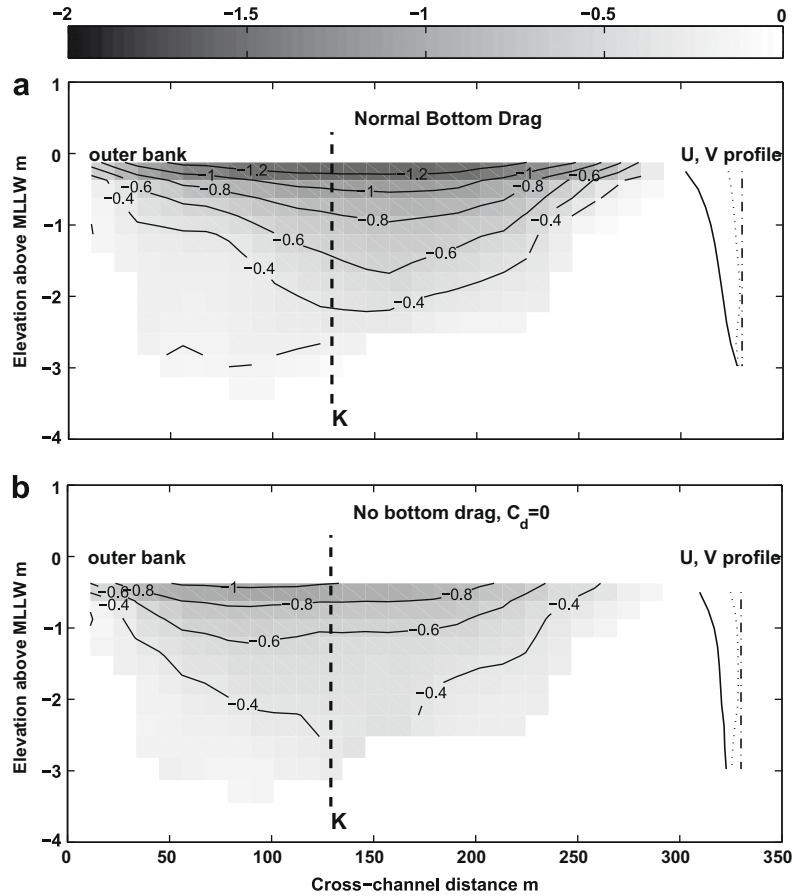
Fig. 15. Profile and contours of streamwise velocity U(m s^{-1}) at transect A-A' (see Fig. 2) from simulations with (a) normal bottom roughness $z_0 = 2.5 \times 10^{-4}$ m and (b) $C_d = 0$ at LLW around year day 193.5. The profiles on the right side of the figures depict the vertical profiles of the streamwise velocity U (–) and transverse velocity V ($\cdots$) at location K. The direction of U is normal to the A-A' transect with positive velocity upstream in the river (into the page); the direction of V is parallel to the transect with positive towards the outer bank (to the left in the figure).

Fig. 16(a) compares the result of the free-surface height at mooring M3b without bottom drag to the original simulation result with bottom drag and the measurements. The effect of removing the bottom drag is to improve the prediction of LLW by lowering it closer to the observations. This is a result of reduced energy dissipation in the absence of bottom friction. Even without bottom friction, however, LLW is still substantially under-predicted. This indicates that numerically-induced dissipation which is predominantly due to the linear ELM scheme may be comparable to and at times greater than the effect of the bottom drag during this stage of the tide.

Fig. 16(b) and (c) show that bottom friction has a much stronger effect on the along-channel, depth-averaged velocities. As shown in Fig. 16(b), although the general behavior of the flow at mooring M3b during strong ebb is relatively unchanged (between year day 193.2 and 193.6), a lack of bottom friction leads to oscillations with periods of roughly three hours and a fluctuation amplitude of roughly 0.8 m s^{-1} that emerge near HHW and slowly decay over the course of the succeeding weak tide (highlighted by the region within the dotted box in Fig. 16). These oscillations are also evident in the signal without bottom drag at mooring M4, as shown in Fig. 16(c). A reduction in the bottom stress allows the tidal energy to propagate to the upstream river boundary and, because it is a clamped boundary that does not radiate any tides, energy is reflected back into the low-friction domain. Assuming a distance of $L = 30$ km from the river mouth to the upstream boundary and an average water depth of roughly $d = 4$ m, the first-mode standing wave frequency in the river is given by $2 L/\sqrt{gd} = 2.7$ h, indicating that the oscillations that appear in the absence of bottom

friction are those due to a standing tidal wave in the main river channel.

As shown in Fig. 16(c), removing the bottom friction also has a strong effect on the along-channel velocity signal at mooring M4. This is indicated by the increased peak ebb current between year day 193.3 and 193.4 and the increase in the peak flood near year day 193.65. Such strong responses in the tidal-scale signals at mooring M4 suggest that bottom friction plays a stronger role in the shallow bypass channel than in the deeper main river channel. Around the time of the strongest ebb flows in the bypass (this is not the peak ebb in the main channel), a large portion of the mudflats in the bypass begins to dry, and the average depth during this time on the mudflats is less than 0.5 m while that in the main river channel is roughly 3 m.

6.3. Nonhydrostatic effects

We can assess the relative importance of the nonhydrostatic pressure in the present simulations by assuming that, away from boundaries where frictional effects are small, the nonhydrostatic pressure acts to make up for a slight imbalance between the barotropic pressure gradient and nonlinear advection of momentum. This imbalance can be analyzed with the two-dimensional steady inviscid equations of motion (neglecting rotation),

$$u\frac{\partial u}{\partial x} + w\frac{\partial u}{\partial z} = -\frac{\partial q}{\partial x} - g\frac{\partial h}{\partial x},$$
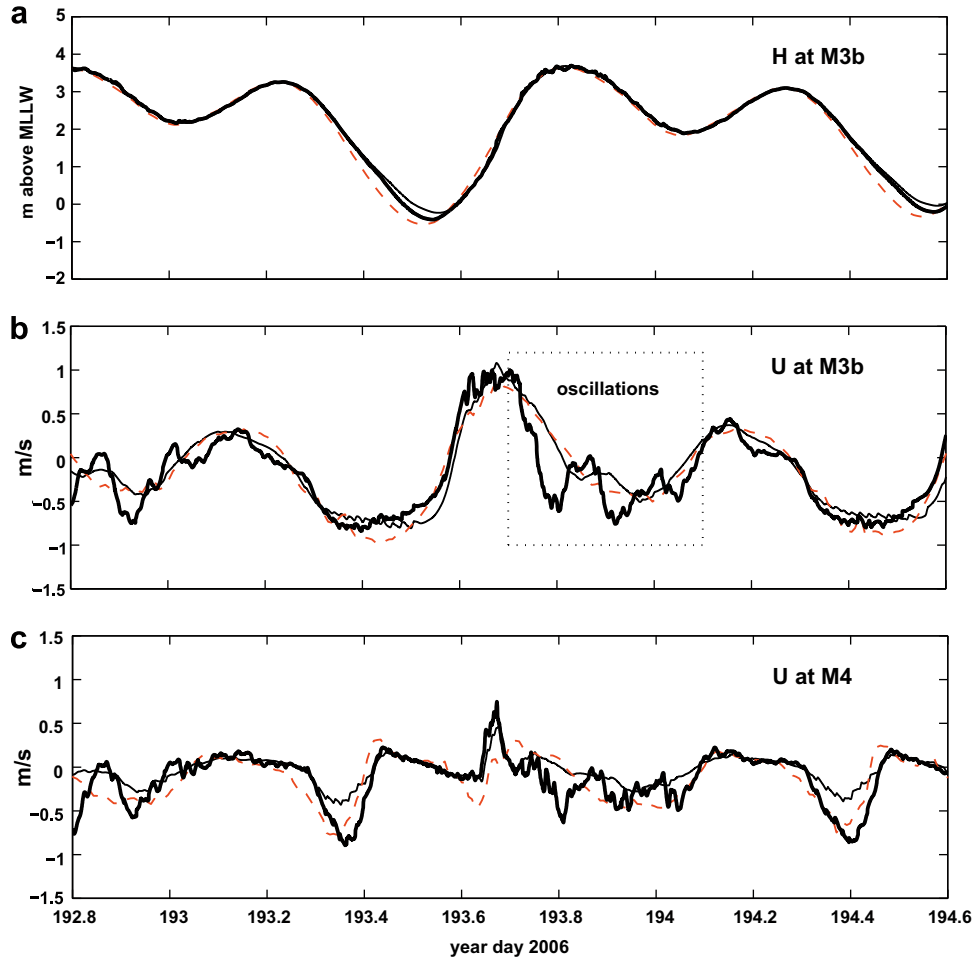$$u\frac{\partial w}{\partial x} + w\frac{\partial w}{\partial z} = -\frac{\partial q}{\partial z},$$

Fig. 16. Time series of (a) free surface and depth-averaged along-channel velocity U at (b) mooring M3b and (c) mooring M4. Legend: simulation with $C_d = 0$ (bold –), the original simulation with normal bottom drag coefficient (thin –), and measurements (thin – –).

where x is the along-channel direction and z is the vertical direction, and u and w are the along-channel and vertical velocities, respectively. If U is the scale for the along-channel velocity, and L and D are scales for the along-channel and vertical variability in the flow (not necessarily the channel geometry), then continuity requires that the vertical velocity scale with $W = \delta U$, where $\delta = D/L$ is the aspect ratio. Choosing a scale for the free surface, H, that imposes a barotropic-nonlinear advection balance then requires $gH = U^2$. If the vertical nonhydrostatic pressure gradient is to balance the vertical advection of momentum, this implies that a scale for the nonhydrostatic pressure is $Q = \delta^2 U^2$. The nondimensional equations of motion are then given by (assuming all quantities are dimensionless)

$$u\frac{\partial u}{\partial x} + w\frac{\partial u}{\partial z} + \frac{\partial h}{\partial x} = -\delta^2\frac{\partial q}{\partial x}, \tag{16}$$

$$u\frac{\partial w}{\partial x} + w\frac{\partial w}{\partial z} = -\frac{\partial q}{\partial z}. \tag{17}$$

This shows that, while the nonhydrostatic pressure is likely not important for large-scale, tidal flow features since $\delta^2 \ll 1$ for these flows, flow features for which $\delta = O(1)$ can be strongly influenced by the nonhydrostatic pressure. Note that different scaling conditions will apply to wave and geostrophic balances (Kanarska et al., 2007).

The tidal flow in the main Snohomish River channel is characterized by an average aspect ratio of $\delta = 10^{-4}$ (along-channel), implying that the flow in the channel is predominantly hydrostatic. The cross-channel length scale is much smaller than the along-channel scale, and corresponds to an aspect ratio of $\delta = 10^{-2}$, indi-

cating that the cross-channel flow may be subject to stronger non-hydrostatic effects. Thus, the focus of the following discussions is on the intratidal transverse flow structures and how they are influenced by the nonhydrostatic pressure. Smaller flow structures are caused by channel curvature, rapidly varying bottom slopes, and channel bifurcation, and the appropriate length scales are those of the flow structures themselves, which lead to larger aspect ratios than that of the channel geometry and nonhydrostaic effects are likely to be stronger. In what follows, we assume that the tidal adjustment occurs over long time scales and the intratidal flow is quasi-steady. We also assume that the advective force balance in Eq. 16 applies in the local hydrodynamics of cross-channel flows (mainly downwelling and upwelling) where nonhydrostatic effects can be considerable.

In order to test the effects of the nonhydrostatic pressure, we performed a nonhydrostatic simulation to compare it to the original hydrostatic simulation. In SUNTANS, the nonhydrostatic pressure-Poisson equation is solved with the predictor–corrector method, which is similar to the methods used by others (e.g., Casulli, 1999; Hodges et al., 2000; Kanarska et al., 2007). Although a block-Jacobi preconditioner substantially decreases the computation time associated with solving the pressure-Poisson equation (Fringer et al., 2006), its solution still incurs an overhead of roughly a factor of two over the hydrostatic simulation. Nevertheless, here we outline its importance with regard to computing small-scale flow features in which the aspect ratio is considerably larger than that of the large-scale channel geometry, and two orders of magnitude greater than that for the along-channel tidal flow.

Fig. 17 depict the transverse velocities denoted by V at four instants in time at transect A-A' (see Fig. 2) for the nonhydrostatic simulation. The contour lines depict the difference in the transverse velocity, ΔV, between the nonhydrostatic and the hydrostatic simulations. Absolute and normalized values of the mean and maximum values of ΔV in the each plot are described in Table 4. As shown in the figure, the flow possesses distinct structures at these points in time that may depend to great extent on the nonhydrostatic pressure. As shown in Fig. 17(a) and (b), a strong shear layer forms during ebb tide in which a layer of strong positive cross-channel flow (positive V) overlies relatively weak cross-channel flow. During the early stages of the ebb tide, as in Fig. 17(a), the flow is stratified, and the shoal on the outer bank of transect A-A' is submerged. The submerged shoal enables water to flow freely over the mudflats in the bypass region and out into the sound, thereby creating a region of large cross-channel flow that forms the upper part of the shear layer. This shear layer slopes upward and is strengthened towards the outer bank of the transect (to the left) as the flow accelerates over the shoal. This accelerating shear layer produces regions in which the hydrostatic and nonhydrostatic simulations differ substantially, as exemplified by the contours of ΔV in this region. An appropriate value of the aspect ratio, δ, for this flow feature is the slope of the shear layer, for which the tangent is roughly 0.04. Although numerous regions with large ΔV exist in the figure that do not coincide with this shear layer, such as along the inner bank of the transect and along the channel bottom, we attribute those to differences arising from processes other than the nonhydrostatic pressure, such as wetting and drying of the shoal, bottom friction, bottom slope, etc, and therefore ignore them in the present discussion.

During late ebb, a region of large positive V exists in the upper part of transect A-A', as shown in Fig. 17(b). However, because the free-surface has dropped, the outer shoal is dry and the channel is disconnected from the bypass. Therefore, rather than being induced by a flow through the bypass, this flow is induced by a recirculating flow due to channel curvature which is modified by transverse bathymetric variability. The recirculating flow is not affected by baroclinic effects since the water column is vertically well-mixed during this stage of the tide. As shown in Fig. 17(b), a return flow exists at depth with a downwelling flow near the outer shoal. Large values of ΔV exist where upwelling and downwelling motions are strongest, and the aspect ratio of these regions appears to be $O(1)$, indicating that they are likely influenced by the nonhydrostatic pressure. However, because it is difficult to ascertain a precise aspect ratio δ for these regions, we only point out that the aspect ratio of the recirculation cell which drives these small-scale motions, which is likely a lower-bound for δ, is roughly 0.03, and this is twice the aspect ratio that would be dictated by the channel cross-sectional geometry.

Fig. 17(c) and (d) depict transverse flow profiles during flood tide. Fig. 17(c) represents the transverse flow at a time during the existence of the axial front that forms at the confluence of the flows from the bypass and the main channel, which features two counter-rotating cells beneath the front as discussed in Section 5. As expected and based on the discussion of the flow during late ebb, Fig. 17(c) shows that the contours of large ΔV are highly correlated with the regions of strong flow convergence due to the recirculating cells. The length scales of these recirculation cells are roughly 50 m in the horizontal and 4 m in the vertical, corresponding to a value of $\delta = 0.08$, which is significant in such a shallow channel flow. Fig. 17(d) is plotted during late flood, when the outer shoal of the transect is well inundated and water flows from the bypass into the main river channel, inducing a flow towards the inner bank in the upper part of the water column. This flow is in the opposite sense of the flow during early ebb, during which time water flows towards the outer bank and into the bypass region, as
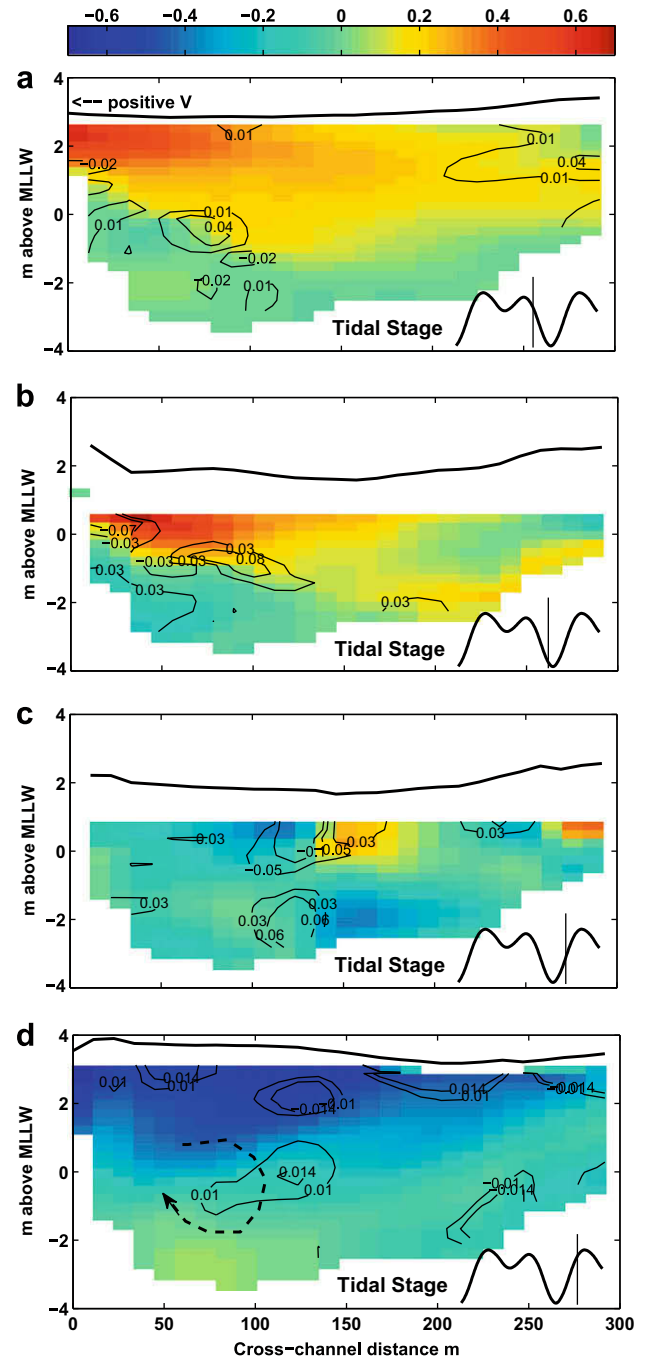

Fig. 17. Profiles of transverse velocity V (m s^{-1}) at transect A-A' (Fig. 2) from the nonhydrostatic simulation. Contours depict the difference (ΔV) between the nonhydrostatic and hydrostatic simulations. The free surface deflection (thick black –) is exaggerated by a factor of 50 in the vertical to illustrate the cross-channel free-surface gradient. The arrow (– –) in (d) indicates the circulation in the separation zone. Tidal stages are depicted in the lower-right corner of the figures. The positive direction of V is parallel to transect A-A' and points toward the outer bank (to the left in the figure).

Table 4
Mean and maximum values of ΔV (m s^{-1}), the difference in the cross-channel velocity between hydrostatic and nonhydrostatic simulations depicted in Fig. 17

Figure	δ	max (ΔV)	$(\Delta V)_{rms}$	V_{rms}	max $(\Delta V)/V_{rms}$	$(\Delta V)_{rms}/V_{rms}$
(a)	0.04	0.04	0.008	0.19	0.21	0.04
(b)	0.03	0.08	0.025	0.19	0.42	0.13
(c)	0.08	0.10	0.029	0.17	0.59	0.17
(d)	0.02	0.02	0.008	0.30	0.03	0.03

depicted in Fig. 17(a). The currents from the main channel and the bypass that converge to produce the flow in Fig. 17(d) form a slightly-sloped layer of relatively large vertical shear, with the channel flow concentrated at depth near the inner bank producing a core of faster longitudinal velocity. It is likely that this results from the discordant depth of the channels at the confluence, where the lateral shear layer is tilted towards the deeper part of the channel (Best and Roy, 1991). Furthermore, the flow from the bypass is slightly less saline than the flow in the main channel by roughly 2 psu (see Fig. 11(f)), and gravitational circulation may intensify the effects of the discordance. As a result, by the time the confluent flows reaches this transect, the shear layer has become almost horizontal. The characteristic aspect ratio of the flow is estimated based on the slope of this shear layer, which is roughly $\delta = 0.02$.

In addition to the shear layer that develops during late flood, Fig. 17(d) depicts a weak circulation cell that has developed at depth near the outer bank, which is a result of flow separation associated with the bypass flow. This feature is common at the opening of a shallow tributary at its junction with a deeper main channel (Best and Roy, 1991; De Serres et al., 1999). Despite the complexity of the flow, contours of ΔV are sparse with small magnitudes, indicating that the transverse flow along transect A-A′ is predominantly hydrostatic because of a lack of structures with constrained horizontal scales and larger values of δ. To conclude, the results in Fig. 17(a–d) and Table 4 show that stronger nonhydrostatic effects are mainly dependent upon the small-scale structures present in the flow and not on the geometry of the flow boundaries. That is, while the geometry might indicate that the flow should become more nonhydrostatic during high water events because of the greater depth, these results indicate that this is not necessarily the case, since small-scale, and hence nonhydrostatic, flow features can appear during any phase of the tidal cycle.

Fig. 18 compares the tidal variations of free-surface height and depth-averaged velocities at mooring M3b from the nonhydrostatic and hydrostatic simulations. The figure shows that the effect of the nonhydrostatic pressure on these quantities is negligible, with a maximum difference in the free-surface height being 0.02 m during strong flood (shown in the figure), and maximum difference in

along-channel velocity and cross-channel velocity being of order 0.05 m s^{-1} during the time of peak flood currents. Recall that mooring M3b is located near the inner bank, where nonhydrostatic activity is weak in general as shown in Fig. 17. Although the nonhydrostatic pressure can have a stronger, localized effect in certain regions of the flow, it does not accumulate over time and has a minimal effect on the large-scale behavior of the flow. This can be expected from the small aspect ratio, δ, of the main-channel geometry, which thus seems to be an adequate indicator of the overall importance of the nonhydrostatic pressure on the large-scale hydrodynamics.

While the physical aspect ratio, δ, is a measure of the relative importance of the nonhydrostatic pressure, the grid aspect ratio, which is the ratio of the vertical to horizontal grid spacing, or $\delta_g = \Delta z/\Delta x$, plays an important role in determining the computational overhead and the numerical error in computing the nonhydrostatic pressure. Here we discuss guidelines for choosing appropriate values for δ_g based on the physical aspect ratio of the nonhydrostatic flow features that are being computed.

Because the Poisson equation in SUNTANS is solved using a second-order accurate finite-difference method to approximate the second-order derivatives, one can show that the leading error (*LED*) is given by (in x and z dimensions on a Cartesian mesh, for simplicity)

$$LED = \frac{1}{12}\left(\Delta x^2 q_{xxxx} + \Delta z^2 q_{zzzz}\right), \tag{18}$$

where q_{xxxx} and q_{zzzz} are the forth-order derivatives of q with respective to x and z. Cross derivatives do not appear because the dimensions are decoupled in the Poisson equation. After normalizing x by L, z by D, and q by Q, the leading error in nondimensional form is given by

$$LED = \frac{Q}{12}\frac{\Delta z^2}{D^4}\left(\frac{\delta^4}{\delta_g^2}q_{xxxx} + q_{zzzz}\right),$$

where it is assumed that the quantities are dimensionless and $q_{xxxx} = O(1)$ and $q_{zzzz} = O(1)$. As previously discussed, the physical
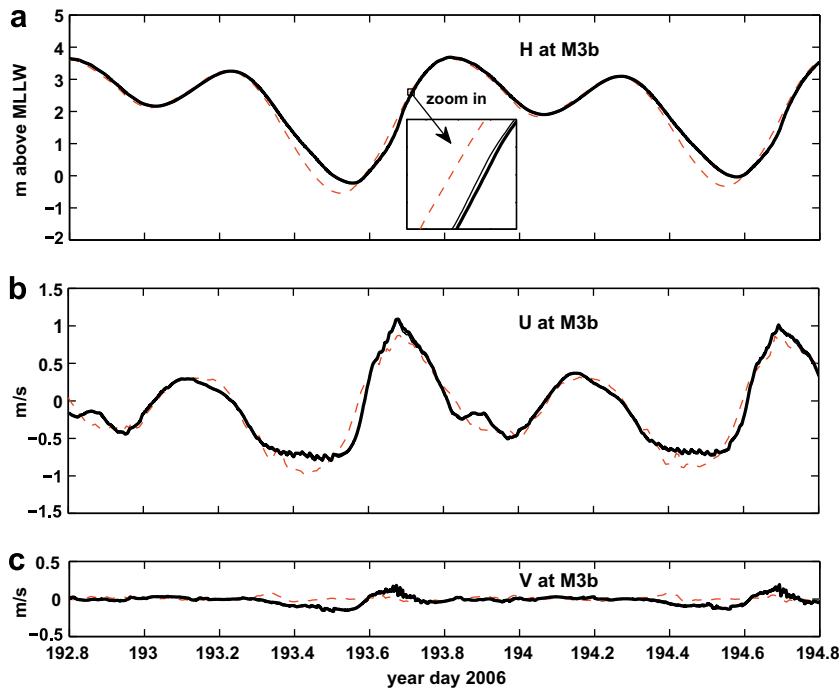

Fig. 18. Time series of (a) free surface, (b) depth-averaged along-channel velocity U and (c) depth-averaged cross-channel velocity V at mooring M3b. Legend: nonhydrostatic simulation (bold –), original hydrostatic simulation (thin –), and measurements (thin – –).

aspect ratio $\delta = D/L$ is dependent upon the nonhydrostatic flow structures of interest. Assuming that the vertical resolution Δz is chosen in order to resolve the vertical structure of the tidal flow in shallow estuaries, then the optimal choice for Δx is one which does not incur a large error associated with computing the horizontal second derivative. This requires that $\delta^2/\delta_g \leqslant 1$, or

$$\delta_g \geqslant \delta^2, \tag{19}$$

which implies that the grid aspect ratio must be at least as large as the square of the physical aspect ratio. In unstructured grid problems with z- or sigma-levels, it is usually straightforward to increase the vertical resolution without drastically increasing the computational overhead, because water columns are usually stored in one-dimensional arrays that are contiguous in main memory. However, since the horizontal extent of most domains is usually quite large it can be taxing to increase the horizontal grid resolution. Furthermore, as discussed by Fringer et al., 2006, smaller values of δ_g increase the effectiveness of the nonhydrostatic preconditioner on the pressure-Poisson equation. Therefore, it is useful to place an upper bound on the horizontal grid spacing in order to determine the minimum computational resources required to resolve a particular nonhydrostatic flow feature while maintaining the effectiveness of the preconditioner. Eq. (19) shows that, if the horizontal derivatives are not to increase the truncation error in the discretization of the nonhydrostatic pressure, then the horizontal grid spacing must satisfy

$$\Delta x \leqslant \Delta z/\delta^2. \tag{20}$$

As one might expect, this relationship implies that the horizontal grid spacing must equal the vertical grid spacing if $\delta = 1$, since the horizontal and vertical grid spacings must match if the horizontal and vertical scales of motion are equal. However, for typical estuarine problems, such as those employed here, it is evident that Eq. 20 is not very restrictive. For example, the grid aspect ratio in the mesh at transect A-A' (Fig. 2) is roughly $\delta_g = 0.025$ which generously satisfies (19) even for the most nonhydrostatic features in Fig. 17(c), for which $\delta^2 = 0.0064 \ll \delta_g$. It is interesting to note that further increasing the accuracy of the discretization of the pressure solver decreases the power on δ in Eq. 20. For instance, the power approaches unity for an infinite-order accurate discretization, requiring $\delta_g \sim \delta$ and $\Delta x \leq \Delta z/\delta$, which imposes a greater constraint on Δx.

6.4. Effects of advection of momentum

Computing advection of momentum, which represents the convective acceleration of fluid particles, is a difficult numerical task, especially when significant wetting and drying occurs and high accuracy is desired (Oey, 2005; Chen et al., 2003; Casulli and Zanolli, 2007). For estuarine flows, advection of momentum, together with the free-surface gradient and bottom drag, is often the dominant term in the momentum equations, and thus it needs to be carefully included in the governing equations. In this section we will show, through numerical experiments and simple scaling analyses, that advection of momentum is critical for both the tidal and sub-tidal dynamics of estuarine flows. In SUNTANS, advection of momentum is discretized with the ELM scheme (Staniforth and Côté, 1991) as discussed in Section 2.2. Although the methodology is based on a rough linear interpolation, use of the ELM scheme has a significant and favorable impact on the results. In what follows, we compare the results of SUNTANS with and without the use of the ELM scheme. The test case without ELM is referred to as the "linear test", which implies that the nonlinear advection of momentum is neglected, i.e. $\mathbf{u} \cdot \nabla \mathbf{u} = 0$, although we retain the nonlinearity in the depth-averaged continuity equation (5).

Fig. 19 depicts the free surface and depth-averaged along-channel velocities at moorings M3b and M4 from the simulations in comparison with the measurements. As shown in Fig. 19(a), the water level during LLW is substantially lower for the linear simulations (bold solid line) than it is for the nonlinear simulation (thin solid line). The water level is so low that it exceeds (is lower than) the measurements and actually approaches the water level offshore in the sound, and the strong ebbs have become symmetric. Similar behavior in the free surface occurs along the entire Snohomish River. At USGS gage station 12150000 (location shown in Fig. 1(a)), observations show that the free surface there is roughly 1 m higher than the offshore water level in the sound at LLW (Fig. 5), which roughly corresponds to a free-surface gradient of 0.05 m km^{-1}, due to the dissipation of tidal energy from various sources. While the nonlinear simulation predicts the free-surface gradient at a correct order of magnitude, the linear simulation substantially under-predicts it. Furthermore, as shown in Fig. 19(b), the currents in the main channel are largely over-predicted in the linear simulation. We can see that the peak ebb current reaches a velocity of 2 m s^{-1}, which is effectively draining the estuary as the tide propagates without much dissipation. Due to the lack of inertial effects associated with nonlinear advection, the ebb flow quickly changes its direction after the flood initiates. The succeeding flood current is also much stronger (up to 2 m s^{-1} with a 3 m s^{-1} sharp peak) as a result of the lowered free surface in the estuary at the end of the ebb tide.

The predicted velocity structure in the linear simulation is also very different from that in the nonlinear simulation. As shown in Fig. 20, the cross-sectional profiles of the along-channel velocity indicate a stronger shear near the bottom and the shoals when nonlinear advection of momentum is ignored. This results because of the lack of transport of slow-moving fluid from the walls to the interior of the flow, and not because of the lack of momentum diffusion since, aside from the inclusion (or lack thereof) of momentum advection, both simulations employ identical parameters.

The strong currents in the linear simulation produce oscillations with magnitudes of roughly 1 m s^{-1} and periods of roughly 1 h during peak flood, and these gradually decay during the subsequent weak tide. Although these oscillations have some similar features to those present in the frictionless simulation as discussed in Section 6.2 (see Fig. 16), they are generated via distinct and more complex mechanisms. The predicted free surface shows that strong flood tides from Steamboat Slough develop into shock waves (we refer to these features as 'shock waves' rather than 'hydraulic bore waves' because of the lack of nonlinear advection of momentum) in the main channel both upstream and downstream of the junction of the slough and the main channel as illustrated in Fig. 21. These shock waves emerge due to the strong tides and the shallow depth in the main channel (it is less than 0.3 m around the junction of the slough) and are the main cause of the oscillations. Note that in the linear simulation, as previously mentioned the solution of the free surface is still nonlinear in the sense that the equation for the free surface (Eq. 5) is obtained by integrating the continuity equation (Eq. 4) from the bottom at $z = -d$ to the actual free surface, where $z = h$. This leads to steepening dynamics that cause wave steepening because wave crests travel faster than troughs, even though advection of momentum is not computed. Another contributor to the strong oscillations occurs at the bypass. When this area becomes submerged, there is a strong impulsive flow of 2 m s^{-1} from the bypass into the main channel (indicated by arrows in Fig. 21) which leads to the formation and propagation of shocks.

Dissipation is insufficient and the resulting currents are too energetic in the linear simulation, and this results from both physical and numerical reasons. Here we analyze the longitudinal momentum equation to assess the relative effects of ignoring
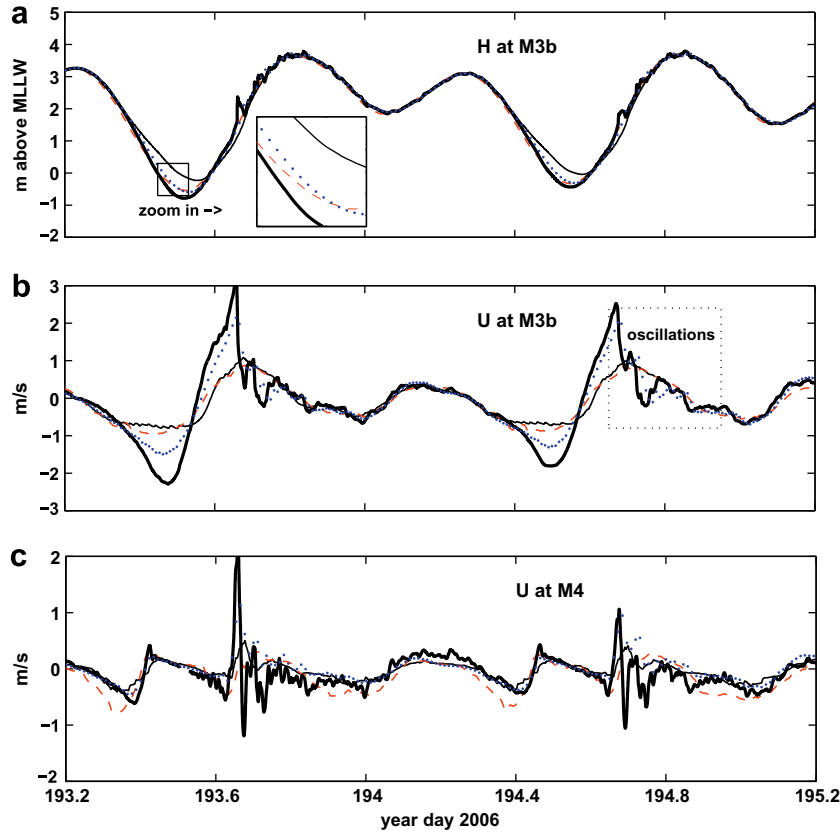
Fig. 19. Time series of (a) free surface, and depth-averaged along-channel velocity U at (b) mooring M3b and (c) mooring M4. Legend: linear simulation with the same viscosities as the nonlinear simulation (bold –), linear simulation with increased viscosities (bold ···), original nonlinear simulation (thin –), and measurements (thin – –).

momentum advection. After ignoring horizontal viscosity, rotation, and nonhydrostatic effects, the main along-channel, or longitudinal momentum balance is given by

$$\frac{\partial U}{\partial t} + U\frac{\partial U}{\partial x} = -g\frac{\partial h}{\partial x} - \frac{C_d}{D}|U_b|U_b, \qquad (21)$$

where U represents the along channel velocity, h is the free-surface height, and D is the water depth. For steady flow, this simplified balance resembles the Bernoulli equation with the kinetic energy term, the potential energy term and frictional energy loss. Rough estimates of the magnitude of the terms based on observations at mooring M3b and USGS gage station 12150000 (Fig. 1) are given in Table 5.

As shown in the table, while the frictional term is predominantly in balance with the free-surface gradient, the effects of unsteadiness and advection of momentum are of comparable magnitude, and the sum of all terms requires a free-surface gradient in the upstream direction along the channel. Neglecting the advection term $\left(U\frac{\partial U}{\partial x}\right)$ will directly lead to an under-prediction of free-surface gradient. Another important finding from the momentum balance is that the actual free-surface gradient notably exceeds the sum of other terms which are already upper-bound estimates. This implies that there may be considerable dissipation due to other mechanisms that are not included in Eq. (21). One of the missing dissipation processes as discovered by earlier studies is the lateral mixing of momentum by advective transverse flows. Cross-channel circulation can develop from channel curvature (Geyer, 1993; Chant, 2002), lateral bathymetric variation (Valle-Levinson and Atkinson, 1999; Valle-Levinson and Li, 2000), and/or baroclinic effects of differential advection of the stream-wise salinity gradient (Wong, 1994; Ralston and Stacey, 2005). The stirring effect of these trans-

verse flows is to intensify the dissipation of energy by bringing the slowly moving flow in the shallows into the interior, which was suggested to have considerable influence on the stream-wise momentum balance (Geyer et al., 2000; Trowbridge et al., 1999). In the linear test, the advective effect of these transverse flows is not presented because $V\frac{\partial U}{\partial y}$ is always zero.

From a numerical point of view, the linear simulation may not have sufficient friction and dissipation because these effects are reduced in the absence of the numerical diffusive effects of momentum advection using ELM. Therefore, in order to test whether it is possible to simulate the numerical effects of ELM using elevated diffusivities alone, a second linear test was performed with increased viscosities that exceed the physical values estimated in Section 2.2. Namely, the horizontal viscosity was increased from 0.01 to 2 m^2 s^{-1} and the molecular viscosity used by MY2.5 to compute the vertical viscosity was increased from 10^{-5} to 10^{-3} m^2 s^{-1}. The results of free surface and depth-averaged velocities are shown in Fig. 19 with thick dotted lines. In these simulations the peak currents are reduced by 30% to 50% relative to those in the previous linear simulation, but they are still very different from the field measurements. Comparing the linear simulation results to the field measurements, we hypothesize that a substantial part of the difference is caused by missing the physical, rather than the numerical, effects of advection of momentum (including inertia and stirring, etc) which are also found to be important in the longitudinal momentum balance in the preceding scaling analysis. However, we are unable to quantify the advective effects more accurately with our current results because it is difficult to separate the physical advective effects of ELM from the associated numerically diffusive effects in the nonlinear simulations.
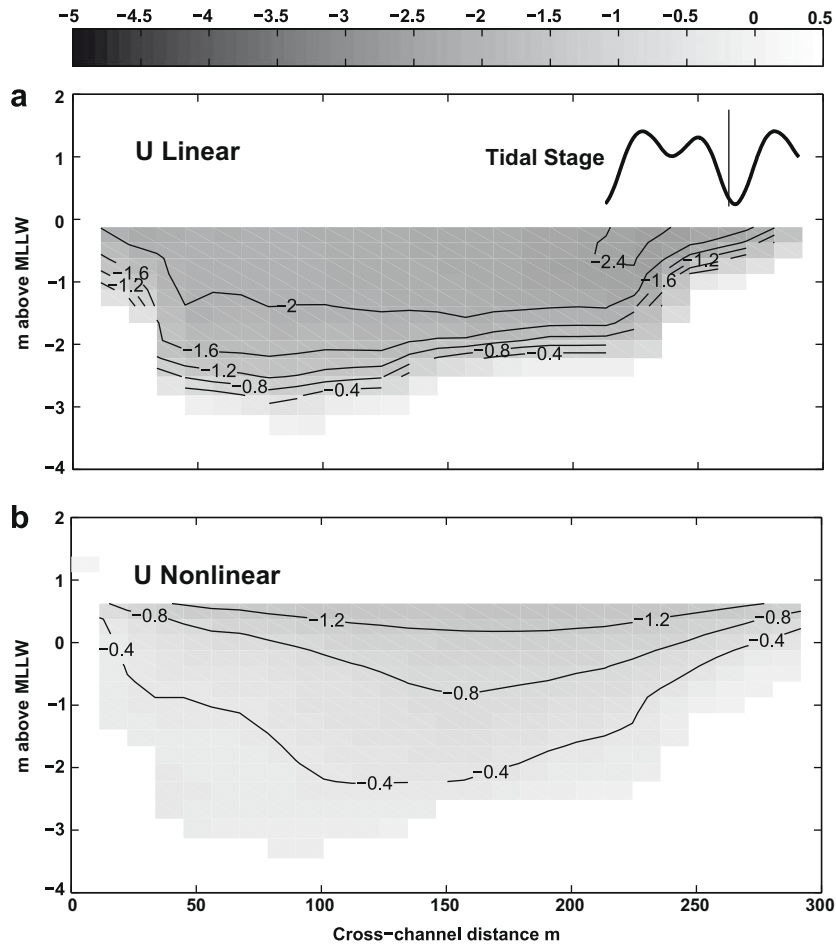
Fig. 20. Profile and contours of along-channel velocity U (m s^{-1}) at transect A-A′ (Fig. 2) from (a) linear simulation, and (b) original nonlinear simulation. The positive direction of the streamwise velocity is normal to transect A-A′ and points upstream (into the page).
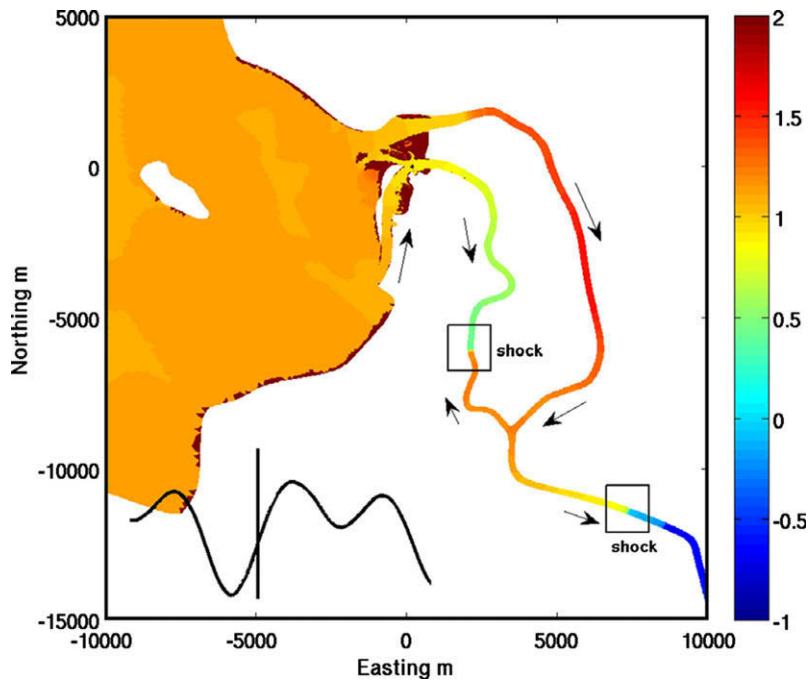
Fig. 21. Free surface (m above MLLW) prediction for the linear simulation showing the development of shock waves in the main Snohomish River channel. Arrows indicate propagation direction of the flood tide.

Table 5
Scaling for the terms in Eq. 21 during strong ebbs based on observations at mooring M3b and USGS gage station 12150000.

$\frac{\partial U}{\partial t}$	$U\frac{\partial U}{\partial x}$	$-g\frac{\partial h}{\partial x}$	$-\frac{C_d}{D}|U_b|U_b$
-0.5×10^{-4}	-0.5×10^{-4}	-5×10^{-4}	2×10^{-4}

Units in the table are in m s^{-2}. A horizontal length scale $L \sim 20$ km is applied, which is the distance between mooring M3b and the gage station. A bottom drag coefficient of $C_d = 2.5 \times 10^{-3}$ obtained from measurements was used for the drag term and the corresponding measured bottom velocity is $U_b = 0.5$ m s^{-1} which is the measured bottom velocity corresponding to the C_d value Giddings et al., 2008. Approximations for the unsteady term, the advection term, and the drag term are all upper-bound estimates using the velocities at the lower part of the estuary.

Advection of momentum also plays a critical role in the cross-channel flow dynamics of curvature-induced secondary circulation. Secondary circulation is not only important to local erosion and sediment transport processes, but also the overall mixing of momentum and scalars in an estuary (Smith, 1976; Trowbridge et al., 1999). Comparison of transverse velocity profiles for the linear and nonlinear simulations shows that the linear simulation fails to capture curvature-induced secondary circulation. The centripetal force of curving stream-wise flow is the dominant forcing to drive the cross-channel circulation (Chant, 2002). It originates from the advection of momentum, $\mathbf{u} \cdot \nabla \mathbf{u}$, and thus is not represented in the linear simulation. Fig. 22 depicts the cross-channel velocity profile at transect A-A′ (location shown in Fig. 2), Fig. 22(a′) shows the circulation due to the curvature of the channel during ebb (same as Fig. 17(b)), and Fig. 22(b′) shows the counter-rotating cells at the bypass confluence during flood (same as

Fig. 17(c)). While circulation cells are apparent in the nonlinear simulation at both times, there is no clear circulation pattern in the linear simulation. To verify that this is the result of omitting advection of momentum rather than due to different mean flow conditions in the two simulations, a linear test was performed by restarting a simulation using the nonlinear results in Fig. 22(b′) as the initial conditions. The results (not shown) show that while the circulation intensifies with time in the nonlinear simulation, it vanishes within 30 min in the linear test and a new equilibrium state is established with a structure similar to that in Fig. 22(b) (not shown).

6.5. Uncertainties in the freshwater inflow

In partially-stratified estuaries, as in the Snohomish River estuary, stable stratification and strong mixing may occur periodically with the tides via strain-induced periodic stratification (Simpson et al., 1990). This mechanism has a significant influence on the flow structure, salinity intrusion and mixing level in the system (Nunes Vaz et al., 1989; Monismith et al., 2002), and will certainly affect the formation of small-scale structures in the flow which is the ultimate interest of the present high-resolution model. It is known that the onset and strength of the stratification is much more sensitive to the freshwater inflow in partially-stratified estuaries than it is in strongly-stratified or well-mixed estuaries (Parker, 1999). Therefore, it is important to have a correct specification of the river flow in numerical models of estuarine hydrodynamics. This, however, is not an easy task in the presence of complex tributary networks which are common in deltas and coastal wetlands.
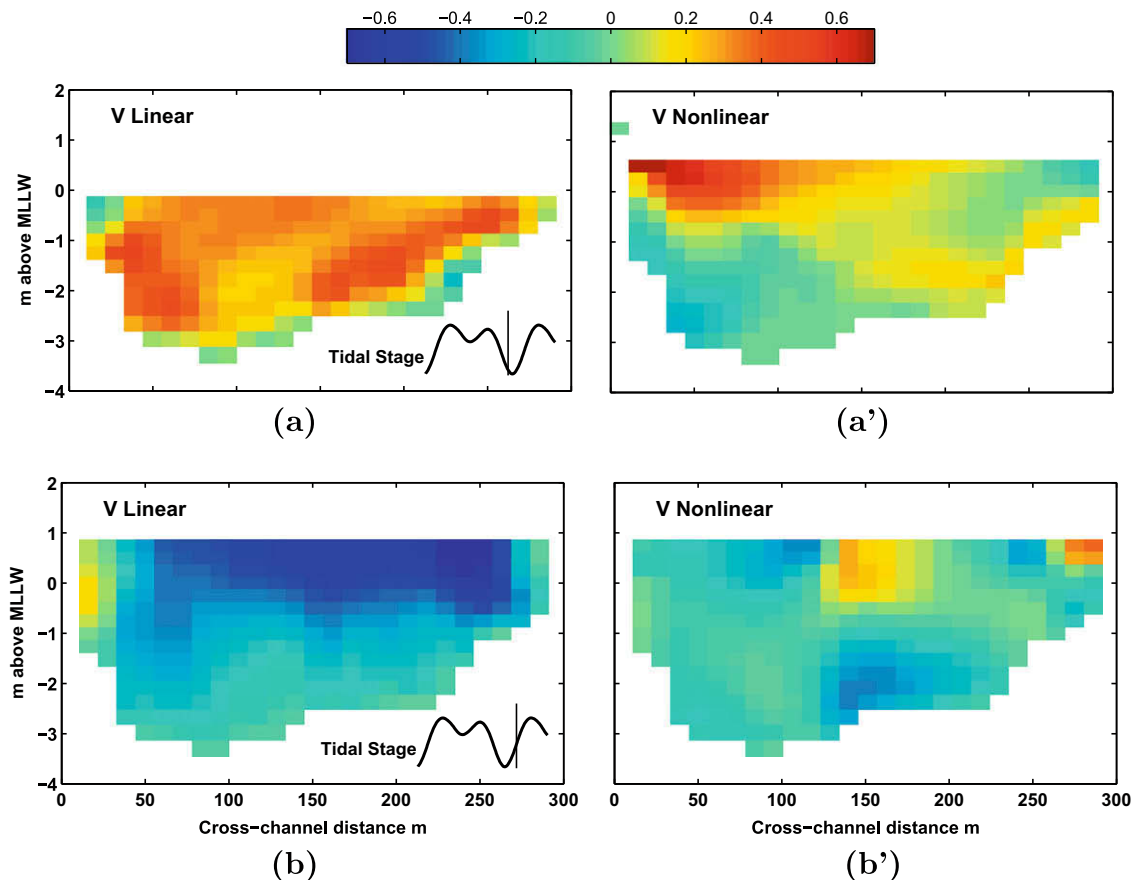

Fig. 22. Profile of transverse velocity V (m s^{-1}) at transect A-A′ (see Fig. 2) during a strong ebb (a) in the linear simulation and (a′) the nonlinear simulation, and during a strong flood (b) in the linear simulation and (b′) in the nonlinear simulation. The positive direction of the transverse velocity is parallel to transect A-A′ and points to the outer edge of the bank (to the left in the figure).

Calibration of overall freshwater inflow and its distribution in the tributaries is difficult because quantities, such as free-surface height, depth-averaged velocities, etc, which are commonly used for calibration purposes, may be insensitive to freshwater inflow, while quantities such as salinity or stratification are strongly influenced by the performance of the turbulence model.

In order to assess the sensitivity of the system to freshwater inflow, a numerical experiment was performed with three times the normal river flow while all other parameters were kept unchanged. As depicted in Fig. 23, while increasing the freshwater inflow leads to a slightly higher free-surface height during LLW, an increase in ebb currents, and a decrease in flood currents at mooring M3b, these differences are small. The strengthening of the ebb flow and weakening of the flood flow directly results from the increase in net downstream flux due to the river flow. The stronger damping of the free-surface variation at LLW is most likely caused by the increase in the peak ebb current, which leads to higher dissipation from a variety of sources and thus requires a larger longitudinal free-surface gradient based on the momentum analysis with Eq. 21. These results demonstrate that the overall effect of increasing the freshwater inflow by a factor of three on the dynamics of the free surface and depth-averaged velocities is very weak and the differences are on the same order as the errors in the simulation. This is to be expected since the tidal fluxes dominate the barotropic dynamics in this macro-tidal system with a tidal range of over 4 m.

While the effect of the freshwater inflow on the free-surface height and depth-averaged currents is weak, differences in the salinity and stratification are much more pronounced. As depicted in Fig. 24, periodic stratification persists even after increasing the freshwater inflow. During the strong ebb tide, when the flow is vertically well-mixed, the salinity at mooring M3b with an increased freshwater inflow is significantly lower and remains fresh for roughly 3 h. The salinity with the normal river flow, on the other hand, only reaches a minimum of 5 psu. The top salinity is 10–20 psu lower, while the bottom salinity is roughly 3 psu lower than that in the original simulation. These variations in the salinity demonstrate that the freshwater inflow induces a stratification

that is twice as strong (measured as the bottom-top salinity difference) during the weak tide.

The weak dependence of the bottom salinity on the increased freshwater inflow is consistent with the analysis of Monismith et al., 2002, which demonstrates that the distance of the salt intrusion upstream of the estuary mouth at depth depends on the freshwater inflow to the $-1/7$ power. The response of the stratification dynamics to changes in freshwater input in the model relies heavily on how well the turbulence closure scheme predicts the level of mixing and its suppression due to stratification. The results imply that the MY2.5 turbulence model can predict the periodic stratification and its adjustment to changes in the freshwater flow reasonably well in a qualitative sense. However, we note that it is difficult to use stratification predictions to calibrate the freshwater inflow because the dynamics are very nonlinear and non-monotonic. That is, it is not possible to tune the flow rate that gives the correct salinity prediction without tuning the turbulence closure and/or modifying other model parameters, such as bottom friction and the horizontal mixing coefficient. This is demonstrated in the results, which show that the strength of stratification is well-predicted in the simulation with normal flow rate, while the bottom salinity during strong ebbs is well predicted with the increased flow rate. Difficulties in calibration based on the salinity are further magnified by uncertainties in the turbulence closure scheme.

7. Summary and conclusions

In this paper, we have presented the setup and validation of a high-resolution numerical model for the Snohomish River estuary, which has been developed to resolve the small-scale intratidal dynamics at the confluence of two river channels in the presence of intertidal mudflats. The model employs the SUNTANS (Fringer et al., 2006) code as the hydrodynamic solver with the modification by Zhao, 2007 which employs the Eulerian–Lagrangian method to enforce stability of momentum advection for shallow water flows. The unstructured grid enables resolution of the complex coastline in the domain and the region of interest while allowing the size of the domain to be large enough to capture large, tidal-scale motions.
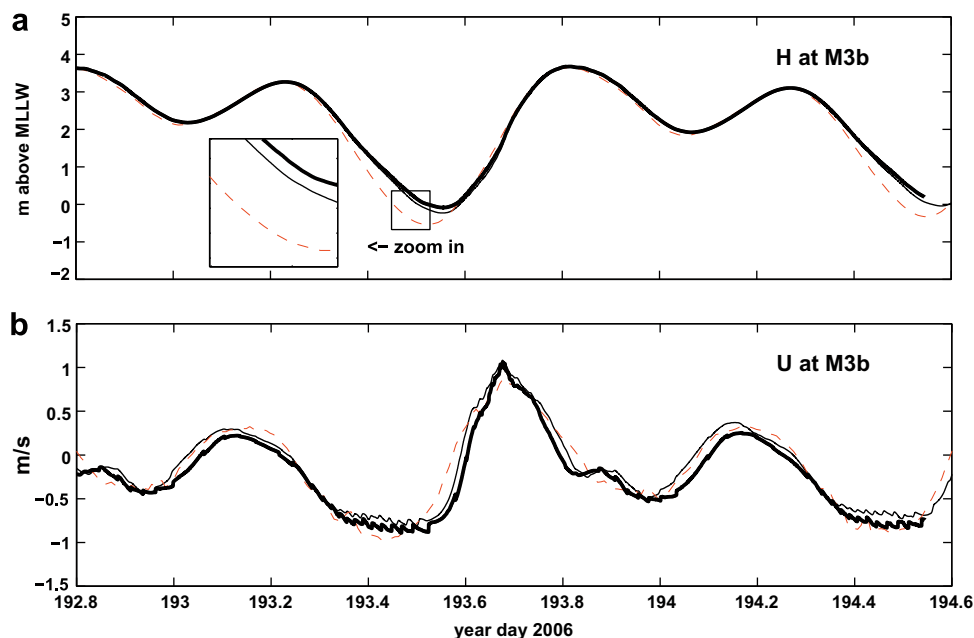

Fig. 23. Time series of (a) free surface and (b) depth-averaged along-channel velocity U at mooring M3b. Legend: simulation with three times the normal river flow (bold –), original simulation with normal river flow (thin –), and measurements (thin – –).
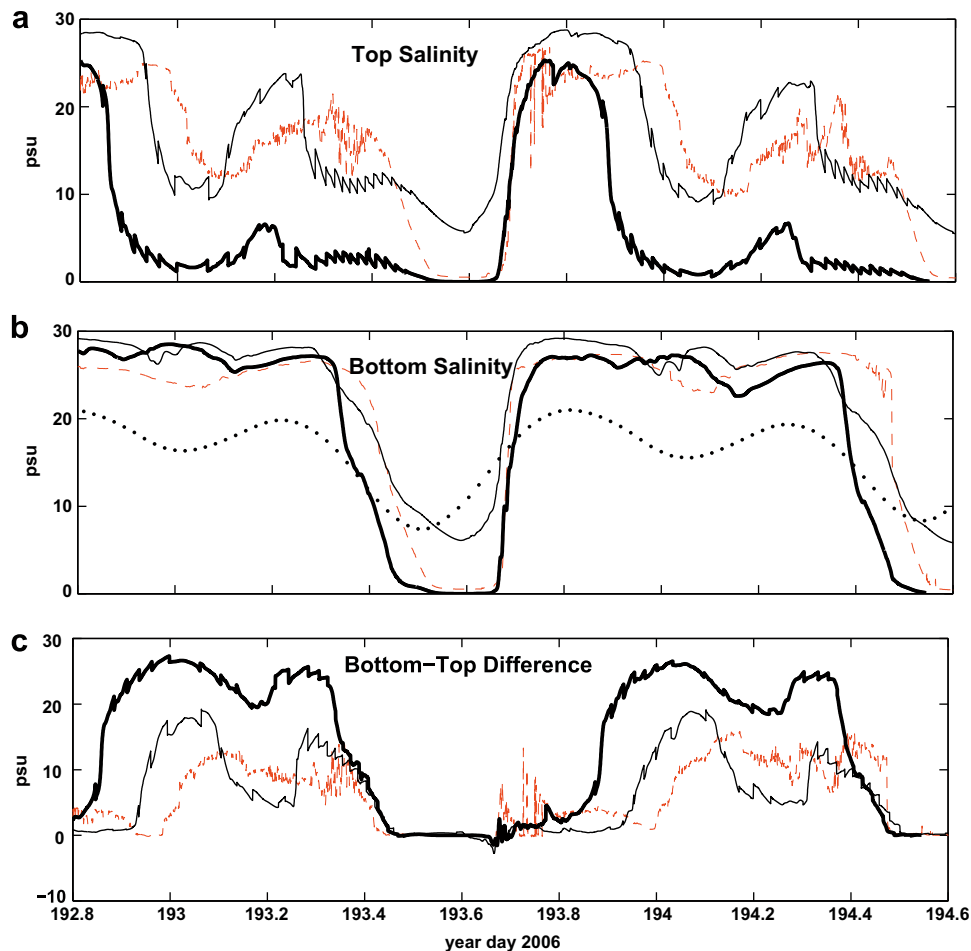
Fig. 24. Time series of (a) top salinity, (b) bottom salinity, and (c) bottom-top salinity difference at mooring M3b. Legend: simulation with three times the normal river flow (bold –), original simulation with the normal river flow (thin –), measurements (thin – –), and tidal stage (. . .).

The predicted free surface and depth-averaged velocities from the model are in good agreement with field measurements, which validate the boundary conditions and parameterizations employed in the model. The small errors in the free surface during LLW and peak ebb indicate that, as expected with an estuarine model, dissipation is overpredicted and is likely a result of errors associated with the first-order ELM scheme used to compute advection of momentum. The salinity prediction captures the periodically stratified characteristic of the estuary with correct top and bottom salinity during weak tides when the fluid is stably stratified, while the prediction for strong ebbs and LLW is less satisfactory. Based on these results, it is likely that the MY2.5 turbulence closure scheme predicts the onset and breakdown of stratification reasonably well for such estuarine conditions. The predicted velocity and salinity fields at the bypass junction show a complex interaction of the tides and the longitudinal salinity gradient with the bypass channel and the intertidal mudflats in the bypass region. This complex flow has significant implications for local mixing, sediment transport and generation of fine-scale flow structures. Examining these processes will be the main objective of a future study in which we plan on employing finer resolution near the study site.

Although high resolution reduces the discretization error associated with the numerical methods employed in the present simulations, it also imposes greater constraints on parameterizations designed to model the effects of subgrid-scale processes. First, and foremost, the present simulations show that accurate bathym-

etry of the intertidal mudflats is critical in predicting correct dynamics of the flow in the bypass. In effect, this implies that an increase in the grid resolution in regions of complex bathymetry cannot come without an increase in the bathymetric resolution. With an increase in bathymetric resolution also comes the necessity of taking greater care in parameterizing the bottom roughness. In particular, the present simulations indicate notable differences in the tidal form (free surface) and currents, particularly over the shallow bypass when different bottom roughness parameterizations are employed. The results also indicate that dissipation from other sources, including channel-shoal exchange of momentum and numerical dissipation, are significant when higher bathymetric resolution is employed.

When high resolution is employed, it also becomes important to consider the potential effects of the nonhydrostatic pressure. Although not necessarily important for the large spatio-temporal scales of the estuarine flow, the simulations show that nonhydrostatic effects may be important for small-scale flow structures in which the relevant aspect ratio can be larger than that dictated by the bathymetric variability. For example, in the present simulations the aspect ratio of the cross-channel bathymetry is $\delta = 0.01$, which would indicate negligible nonhydrostatic effects and is indeed corroborated by the negligible differences in tidal form and depth-averaged velocities at the mooring locations when the nonhydrostatic pressure is computed. However, the aspect ratio of the two-cell circulation beneath the axial front in the water column are much larger at $\delta = 0.08$, and it is in this circulation that significant

differences between the hydrostatic and nonhydrostatic simulations appear.

While the nonhydostatic pressure acts to influence local processes and has a small effect on the large-scale dynamics, advection of momentum has a prominent effect on the tidal form and along-channel, depth-averaged currents. In the linear simulation, which assumes $\mathbf{u} \cdot \nabla \mathbf{u} = 0$, the observed free-surface gradient at LLW is not established and the asymmetries in the tidal form are not present. The linear simulation also predicts unrealistically large velocities. While one might expect that this is due to a lack of numerical dissipation inherent to the first-order accurate ELM scheme, using a straightforward scaling analysis, we have shown that inclusion of the ELM scheme actually acts to increase the physical dissipation associated with nonlinear advection, while the numerical effect is secondary. This is corroborated by the results that show how an increase in the horizontal diffusion coefficient does not capture the correct dissipative dynamics.

Lastly, these simulations show that the effect of the freshwater inflow on the tidal form and currents is very weak, which is reasonable due to the dominance of the tidal fluxes. However, the salinity and stratification predictions are much more sensitive to the change in freshwater input. With increased freshwater inflow, the difference is mainly in the top salinity which becomes substantially fresher, while the bottom salinity only changes slightly. These results show that a reasonable response to increased freshwater inflow can be obtained with the MY2.5 turbulence closure scheme. The simulations presented here, however, indicate that it is not straightforward to calibrate the salinity dynamics by adjusting the fresh river inflow. The barotropic quantities, such as free surface and depth-averaged velocities are insensitive to the river flow, while the baroclinic quantities, such as the salinity and velocity profiles, respond to the river inflow in a complex, non-monotonic way because the development of stratification is inherently nonlinear.

In summary, this paper shows that high resolution is clearly not the only answer to obtaining better match between predictions and observations, particularly for flows in complex macrotidal estuaries. High resolution increases the range of spatio-temporal scales that can be simulated, including scales that are influenced by the nonhydrostatic pressure, and high resolution decreases the overall discretization error, particularly associated with the momentum advection scheme. However, subgrid-scale processes and boundary conditions play a strong role in the dynamics even with high resolution. This should be of no surprise, considering that from a fundamental point of view, simulation of flow in an estuary is a boundary value problem in which the dynamics depends little on the initial conditions but to great extent on the boundary conditions. The most telling evidence of this is that, in the present and most typical simulations, the initial free surface and velocity field are quiescent and the initial salinity field is grossly oversimplified, but these have virtually no effect on the results after a few tidal cycles of spinup time. On the other hand, most of the present work associated with obtaining accurate predictions is related to boundary conditions, including, in order of importance, tidal forcing, bottom bathymetry, bottom roughness, and river inflow. While also important, the turbulence parameterization is secondary because it has the strongest influence on the stratification dynamics but a weaker influence on the tidal form and depth-averaged currents. Ultimately, as the grid resolution becomes further refined, the dependence of the solution on the turbulence model continues to decrease, until the simulation effectively becomes a direct numerical simulation. Even with such exceedingly high grid resolution (which is clearly not tractable even with the most powerful supercomputers at this time), the solution will continue to depend to a large extent on accurate specification of boundary conditions.

References

Ashmore, P.E., 1982]. Laboratory modelling of gravel braided stream morphology. Earth Surf. Proc. Land. 7, 201–255.

Aubrey, D.G., Speer, P.E., 1985]. A study of non-linear tidal propagation in shallow inlet/estuarine systems, Part I: observations. Estuar. Coast. Shelf Sci. 21, 185–205.

Best, J.L., Roy, A.G., 1991]. Mixing-layer distortion at the confluence of channels of different depth. Nature 350, 411–413.

Blumberg, A.F., Mellor, G.L., 1987]. A description of a three-dimensional coastal ocean circulation model. In: Heaps, N. (Ed.), Three-Dimensional Coastal Ocean Models. American Geophyiscal Unoin, pp. 1–16.

Blumberg, A.F., 1993. A primer of ECOM3D-si. Technical report. HydroQual, Inc., Mahwah, New Jersey.

Brooks, D.A., Baca, M.W., Lo, Y.T., 1999]. Tidal circulation and residence time in a macrotidal estuary: Cobscook Bay, Maine. Estuar. Coast. Shelf Sci. 49, 647–665.

Cannon, G.A., 1983. An overview of circulation in the Puget Sound estuarine system. NOAA Technical Memorandum ERL PMEl-48, 30pp.

Casulli, V., 1990]. Semi-implicit finite difference methods for the two-dimensional shallow water equations. J. Comput. Phys. 86, 56–74.

Casulli, V., Cattani, E., 1994]. Stability, accuracy and efficiency of a semi-implicit method for three-dimensional shallow water flow. Comput. Math. Appl. 27, 99–112.

Casulli, V., 1999]. A semi-implicit finite difference method for non-hydrostatic, free-surface flows. Int. J. Numer. Meth. Fluids 30, 425–440.

Casulli, V., Zanolli, P., 2007]. Comparing analytical and numerical solution of nonlinear two and three-dimensional hydrostatic flows. Int. J. Numer. Meth. Fluids 53, 1049–1062.

Chant, R.J., 2002]. Secondary circulation in a region of flow curvature: relationship with tidal forcing and river discharge. J. Geophys. Res. 107, 3131.

Chen, C., Liu, H., beardsley, R.C., 2003]. An unstructured grid, finite-volume, three-dimensional, primitive equations ocean model: application to coastal ocean and estuaries. J. Atmos. Ocean. Technol. 20, 179–186.

Cheng, R.T., Ling, C.H., Gartner, J.W., Wang, P.F., 1993]. Estimates of bottom roughness length and bottom shear stress in South San Francisco Bay, California. J. Geophys. Res. 104, 7715–7728.

Chickadel, C.C., Horner-Devine, A.R., Jessup, A.T., 2008. Thermal remote sensing of boils generated at a submerged estuarine sill. In: Proceedings of AGU Ocean Sciences Meeting, Orlando, Florida, March 2–7, 2008.

De Serres, B., Roy, A.G., Biron, P.M., Best, J.L., 1999]. Three-dimensional structure of flow at a confluence of river channels with discordant beds. Geomorphology 26, 313–335.

Edwards, K.A., Jessup, A.T., 2008. Aircraft temperature measurements in the Snohomish River estuary during COHSTREX. In: Proceedings of AGU Ocean Sciences Meeting, Orlando, Florida, March 2–7, 2008.

Finlayson, D.P., 2005. Combined bathymetry and topography of the Puget Lowland, Washington State. www.ocean.washington.edu/data/pugetsound/.

Fischer, H.B., 1976]. Mixing and dispersion in estuaries. Annu. Rev. Fluid Mech. 8, 107–133.

Fram, J.P., Gerbi, G., Geyer, W.R., MacCready, P., 2003. Longitudinal and lateral salt gradients of the Snohomish River estuary: summer research project at Friday Harbor Laboratories. Eos Trans. AGU, 84(52), Ocean Sci. Meet. Suppl., Abstract OS42A-10.

Fringer, O.B., Gerritsen, M., Street, R.L., 2006]. An unstructured-grid, finite-volume, nonhydrostatic, parallel coastal ocean simulator. Ocean Modell. 14, 139–173.

Galperin, B., Kantha, L.H., Hassid, S., Rosati, A., 1988]. A quasi-equilibrium turbulent energy model for geophysical flows. J. Atmos. Sci. 45, 55–62.

Geyer, W.R., 1993]. Three-dimensional tidal flow around headlands. J. Geophys. Res. 98, 955–966.

Geyer, W.R., Trowbridge, J.H., Bowen, M.M., 2000]. The dynamics of a partially mixed estuary. J. Phys. Oceanogr. 30, 2035–2048.

Giddings, S.N., Fong, D.A., Monismith, S.G., 2008. Mixing and circulation in a macrotidal, shallow estuary. In preparation.

Gross, E.S., 1997. Numerical modeling of hydrodynamics and scalar transport in an estuary. Ph.D. Dissertation, Stanford University. 313pp.

Gross, E.S., Koseff, J.R., Monismith, S.G., 1999]. Three-dimensional salinity simulations of South San Francisco Bay. J. Hydr. Eng. 125, 1199–1209.

Gustafson, R.G., Lenarz, W.H., McCain, B.B., Schmitt, C.C., Grant, W.S., Builder, T.L., Methot, R.D., 2000. Status review of Pacific Hake, Pacific Cod, and Walleye Pollock from Puget Sound, Washington. US Department of Commerce. NOAA Technical Memorandum NMFS-NWFSC-44, 275pp.

Hanert, E., Le Roux, D.Y., Legat, V., Deleersnijder, E., 2005]. An efficient Eulerian finite element method for the shallow water equations. Ocean Modell. 10, 115–136.

Hodges, B.R., Imberger, J., Saggio, A., Winters, K.B., 2000]. Modeling basin-scale internal waves in a stratified lake. Limnol. Oceanogr. 45, 1603–1620.

Ip, J.T.C., Lynch, D.R., Friedrichs, C.T., 1998]. Simulations of estuarine flooding and dewatering with application to Great Bay, New Hampshire. Estuar. Coast. Shelf Sci. 47, 119–141.

Itsweire, E.C., Koseff, J.R., Briggs, D.A., Ferziger, J.H., 1993]. Turbulence in stratified shear flows: implications for interpreting shear-induced mixing in the ocean. J. Phys. Oceanogr. 23, 1508–1522.

Jessup, A., T., Phadnis, K.R., Horner-Devine, A., Hayworth, B., Plant, W.J., 2006. Infrared imagery of flow over a sill in a tidally-influenced river. Eos Trans. AGU, 87(36), Ocean Sci. Meet. Suppl., Abstract OS12E-01.

Kanarska, Y., Shchepetkin, A., McWilliams, J.C., 2007]. Algorithm for non-hydrostatic dynamics in the regional oceanic modeling system. Ocean Modell. 18, 143–174.

Lavelle, J.W., Mofjeld, H.O., Lempriere-Doggett, E., Cannon, G.A., Pashinski, D.J., Cokelet, E.D., Lytle, L., Gill, S., 1988. A multiply-connected channel model of tides and tidal currents in Puget Sound, Washington and a comparison with updated observations. NOAA Technical Memorandum ERL PMEL-84, 103pp.

Lynch, D.R., Gray, W.G., 1980]. Finite element simulation of flow in deforming regions. J. Comput. Phys. 36, 135–153.

McCalpin, J.D., 1988]. A quantitative analysis of the dissipation inherent in semi-lagrangian advection. Mon. Weather Rev. 116, 2330–2336.

Mellor, G.L., Yamada, T., 1982]. Development of a turbulence closure model for geophysical fluid problem. Rev. Geophys. Space Phys. 20, 851–875.

Mellor, G.L., Ezer, T., Oey, L.Y., 1994]. The pressure gradient conundrum of sigma coordinate ocean models. J. Atmos. Ocean.Technol. 11, 1126–1134.

Mofjeld, H.O., Larsen, L.H., 1984. Tides and tidal currents of the inland waters of western Washington. NOAA. Technical Memorandum ERL PMEL-56, 52pp.

Monismith, S.G., Kimmerer, W., Burau, J.R., Stacey, M.T., 2002. Structure and flow-induced variability of the subtidal salinity field in northern San Francisco Bay. J. Phys. Oceanogr. 32, 3003–3019.

Nepf, H.M., 1999]. Drag, turbulence, and diffusion in flow through emergent vegetation. Water Resour. Res. 2, 479–489.

Nunes Vaz, R.A., Lennon, G.W., de Silva Samarasinghe, J.R., 1989]. The negative role of turbulence in estuarine mass transport. Estuar. Coast. Shelf Sci. 28, 361–377.

Oey, L.Y., 2005]. A wetting and drying scheme for POM. Ocean Modell. 9, 133–150.

Pain, C.C., Piggott, M.D., Goddard, A.J.H., Fang, F., Gorman, G.J., Marshall, D.P., Eaton, M.D., Power, P.W., de Oliveira, C.R.E., 2005]. Three-dimensional unstructured mesh ocean modeling. Ocean Modell. 10, 5–33.

Parker, M., 1999]. Estuarine adjustment to changes in river flow and tidal mixing. J. Phys. Oceanogr. 29, 709–726.

Perot, B., 2000]. Conservation properties of unstructured staggered mesh schemes. J. Comput. Phys. 159, 58–89.

Ralston, D.K., Stacey, M.T., 2005]. Longitudinal dispersion and lateral circulation in the intertidal zone. J. Geophys. Res. 110, C07015.

Signell, R.P., Butman, B., 1992]. Modeling tidal exchange and dispersion in Boston Harbor. J. Geophys. Res. 97, 591–606.

Smith, R., 1976]. Longitudinal dispersion of a buoyant contaminant in a shallow channel. J. Fluid Mech. 78, 677–688.

Simpson, J.H., Brown, J., Matthews, J., Allen, G., 1990]. Tidal straining, density currents, and stirring in the control of estuarine stratification. Estuaries 13, 125–132.

Stacey, M.T., Monismith, S.G., Burau, J.R., 1999]. Observations of turbulence in a partially stratified estuary. J. Phys. Oceanogr. 14, 506–527.

Staniforth, A., Côté, J., 1991]. Semi-Lagrangian integration methods for atmospheric models: a review. Mon. Weather Rev. 119, 2206–2223.

Trowbridge, J.H., Geyer, W.R., Bowen, M.M., Williams, A.J., 1999]. Near-bottom turbulence measurements in a partially mixed estuary: Turbulent energy balance, velocity structure and along-channel momentum balance. J. Phys. Oceanogr. 29, 3056–3072.

Valle-Levinson, A., Atkinson, L.P., 1999]. Spatial gradients in the flow over an estuarine channel. Estuaries 24, 179–193.

Valle-Levinson, A., Li, C., 2000]. Convergence of lateral flow along a coastal plain estuary. J. Geophys. Res. 105, 17045–17061.

Walters, R.A., Lane, E.M., Henry, R.F., 2007]. Semi-Lagrangian methods for a finite element coastal ocean model. Ocean Modell. 19, 112–124.

Wang, J., 2005. Non-hydrostatic numerical simulation of littoral internal waves on an unstructured grid. Ph.D. Dissertation, Stanford University. 166pp.

Warner, J.C., Schoellhamer, D.H., Ruhl, C.A., Burau, J.R., 2004]. Floodtide pulses after low tides in shallow submembayments adjacent to deep channels. Estuar. Coast. Shelf Sci. 60, 213–228.

Wong, K.C., 1994]. On the nature of transverse variability in a coastal plain estuary. J. Geophys. Res. 99, 14209–14222.

Zhao, G., 2007. Numerical simulation of complex channel flows. Ph.D. Dissertation, Stanford University. 144pp.

Zheng, L., Chen, C., Liu, H., 2003]. A modeling study of the Satilla River estuary, Georgia. I: flooding-drying process and water exchange over the salt marsh-estuary-shelf complex. Estuaries 26, 651–669.